

# **Radiative Cascades in Semiconductor Quantum Dots**

**Eilon Poem and David Gershoni**

**Department of Physics, The Technion – Israel Institute of Technology, Haifa 32000, Israel**

## ***Abstract***

We review the current understanding of the photoluminescence spectroscopy from single semiconductor quantum dots in general, and radiative cascades as part of it, in particular. We outline in simple terms the theory which is required for understanding few carriers' states confined in semiconductor quantum dots and the selection rules for optical transitions between these states. We then compare the theoretical tools that we developed with measured polarization sensitive photoluminescence spectra. We proceed by discussing the dynamics of confined charge carriers in quantum dots and introduce tools for discussing semi-empirically spin scattering during carriers' thermalization. The spin scattering rates are then deduced by measuring the degree of linear and circular polarization memory during resonant and quasi resonant excitations. We present rate and Master equation models for describing the temporal evolution of the population and coherence of the many carrier states in these nanostructures. Equipped with these tools we discuss polarization sensitive intensity correlation spectroscopy as an experimental tool for probing the dynamics of a system. We conclude this chapter by discussing various biexciton-exciton radiative cascades in neutral and in charged quantum dots.

## ***Introduction***

Semiconductor quantum dots (QDs) are nanometric scale regions of a narrow-bandgap semiconductor embedded within a wider-bandgap semiconductor. They confine charge carriers (electrons and/or holes) in all three dimensions. The QD's energy level spectrum is therefore discrete, much like that of the fundamental building blocks of nature – atoms and molecules.

QDs are therefore often referred to as “artificial atoms” [1- 3]. They have been extensively investigated recently as potential, technology-compatible quantum light emitters [4- 6] providing single photons, or “flying Qubits” on demand. More recently, it has been shown that QDs can emit pairs of entangled photons [7, 8]. Such capabilities are important for possible future applications such as quantum information processing [9] and cryptography [10]. Though similar effects were previously observed in the fluorescence of single atoms and molecules [11], semiconductor QDs offer many advantages. In particular, they exhibit large electrostatic capacitance, which enables a wide range of charge states [12]. This feature, among others, forms a sound base for the QDs’ potential applications. At the same time it makes them an excellent stage for studying inter-charge-carrier interactions in confined spaces.

One of the experimental methods frequently used to investigate single QDs is micro-photoluminescence ( $\mu$ PL). In a  $\mu$ PL experiment, the QD is optically excited by laser light, focused on the QD through a microscope objective. The light emitted by the QD is collected through the same microscope objective and spectrally analyzed by a spectrometer. Spatial filtering using a confocal aperture could be used in order to enhance the spatial resolution. The exciting light promotes an electron from the full valence band, leaving there a hole, to the empty conduction band, thus creating an electron-hole (e-h) pair, or an ‘exciton’. If the excitation is off-resonance, the pair is generated in the vicinity of the QD, and it moves in the semiconductor until it either recombines first, or captured by the QD and only then recombines. Since the energy levels of a QD are discrete, the recombination of an e-h pair in a QD gives rise to a discrete spectral line (See Fig. 1). In analogy to atomic physics, we denote PL lines resulting from the recombination of an e-h pair occupying the first (second, third) single-carrier levels by the letters  $s$  ( $p$ ,  $d$ ).

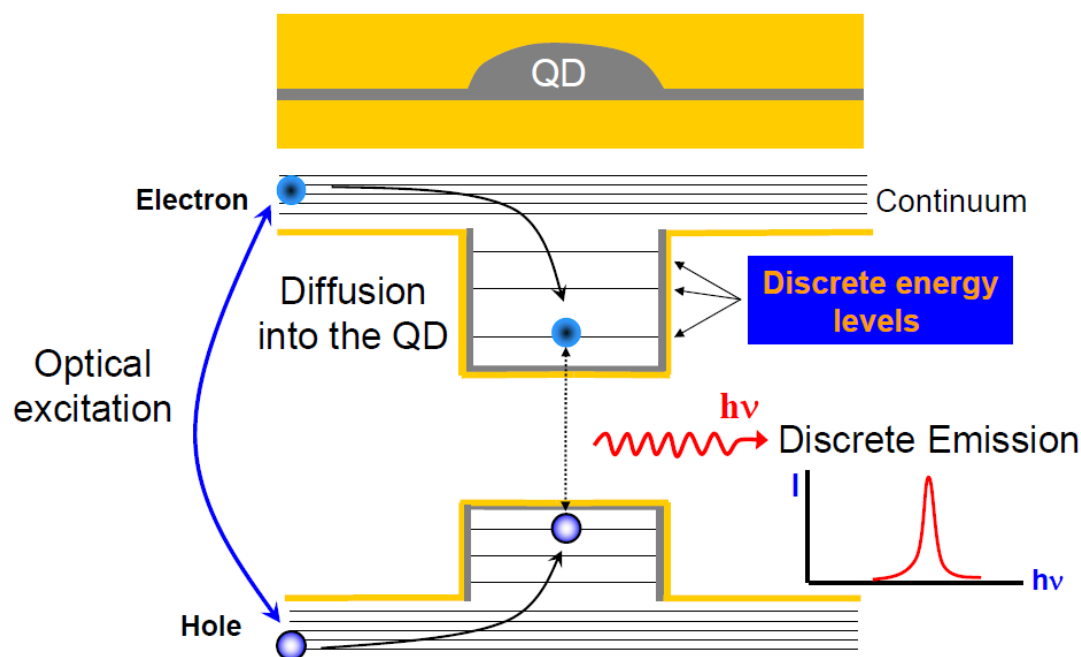


Fig. 1.

Schematic illustration of photoluminescence emission from a single semiconductor QD under non-resonant optical excitation.

A QD may be populated by more than one e-h pair, or populated with an uneven number of electrons and holes. In such cases, the recombination energy of an e-h pair will be affected by the additional Coulombic interactions. Therefore, typically more than one spectral line is seen around the single e-h pair ground state recombination line, as illustrated in Fig. 2.

We name the various transitions as follows: The letter X (for eXciton) is written as many times as there are e-h pairs in the initial state. The number and sign of unpaired charge carriers is written as a superscript after the last X. For example, transitions starting from states which contain 3 holes and 2 electrons will be denoted  $XX^+$ . Additional subscripts may be used to distinguish between different spin configurations of the initial and/or the final states, as will be explained later. The identification of a spectral line is thus the ability to identify an e-h pair recombination process, uniquely defined by its many-body initial and final states.

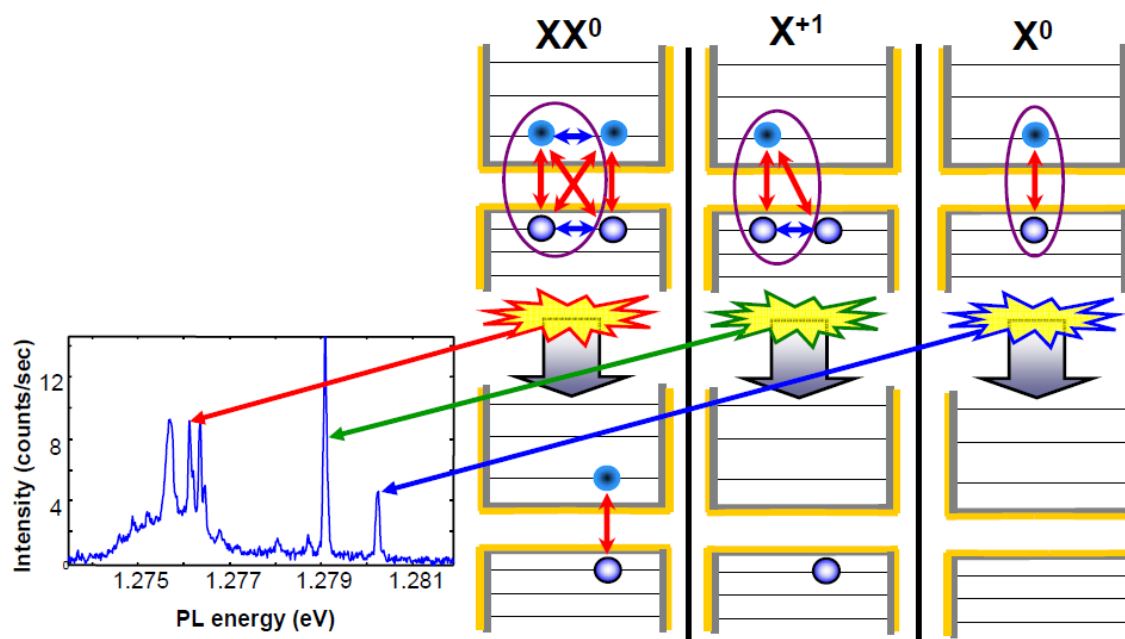


Fig. 2. Schematic description of various radiative pair-recombination processes in the presence of spectator charge carriers. The Coulombic interactions (blue arrow represents repulsion, while red one represents attraction) affect the many body state energies. Therefore, several different spectral lines are expected for the recombination of an s-shell (e-h) pair.

Each of the properties of the line's initial and final configurations can be obtained experimentally: The number of e-h pairs can be deduced from the dependence of the line's intensity upon the excitation power. The number and sign of excess charge carriers can be deduced from experiments in which the charge of the QD is controlled (by means of electrical and/or optical excitations). The spin configurations can be deduced by polarization sensitive spectroscopy and polarization memory experiments. Polarization sensitive intensity correlation measurements can be used in addition, for verification of the line identification and for obtaining additional insight into the dynamical processes by which the excited QD relaxes, including the identification of radiative cascades.

The discussion of these processes is organized as follows: In the first section, we begin with theoretical description of the many-body states and energy levels of QD-confined charge-carriers, and radiative transitions between them. In the second section we present measured polarization sensitive PL spectra of a single QD, and compare it to the theoretically predicted transitions. In the third section we discuss charge carrier dynamics. We present results obtained by polarization memory experiments and present a theoretical model to explain them. We discuss intensity cross-correlation measurements as an experimental tool for probing carrier dynamics, and present the theory behind it. In the last section we discuss the notion of radiative cascades, and present experimentally measured intensity cross-correlation functions which reveal such cascades in both neutral and charged QDs. We show that important information about the dynamical processes can be extracted from these measurements.

### ***Theoretical model for calculating few confined carrier states in semiconductor quantum dots***

The goal of this section is to provide theoretical tools for analyzing the optical spectrum of semiconductor QDs and its polarization selection rules. We provide such a tool by a model which is based on a full-configuration interaction (FCI) method [13-15]. Traditionally, this method provides a straight forward tool for calculating many- indistinguishable interacting carriers' levels from their known single carrier states. Our approach is unique, however, in the sense that it includes also the exchange interaction between the seemingly distinguishable electrons and holes [16-18]. This interaction is orders of magnitude smaller than the exchange interactions between carriers of same charge [17, 18], yet, as we show, it determines the polarization selection rules of the PL spectrum of semiconductor QDs.

The FCI method requires as an input the energies and wavefunctions of single-carrier in the QD

potential. We supply this information both for the electron and for the hole. There are few methods for solving the single carrier problem [19-27]. However, since the actual composition, strain dimensions and shape of a particular QD is not accurately known, we prefer the simplest approach which provides a consistent set of single carrier states, of which a finite set of states is chosen. The interaction energies between pairs of carriers in any one of the chosen states are then calculated. For the Coulomb interaction, these elements are given by,

$$C_{n_1, n_2, n_3, n_4}^{p_1 p_2 p_3 p_4} = \iint d^3 r_1 d^3 r_2 \psi_{n_1}^{p_1*}(\vec{r}_1) \psi_{n_2}^{p_2*}(\vec{r}_2) \frac{e^2}{\epsilon |\vec{r}_1 - \vec{r}_2|} \psi_{n_3}^{p_3}(\vec{r}_2) \psi_{n_4}^{p_4}(\vec{r}_1) \quad (1.1)$$

where  $e$  is the electron charge,  $\epsilon$  is the dielectric constant,  $p_{1..4}$  can be either 'e' (for electron) or 'h' (for hole), and the indices  $n_{1..4}$  run over the appropriate single particle states.

At this stage, in order to insure convergence, it should be verified that the interaction elements which connect low energy states to higher energy states are smaller than the energy differences between these states. For a QD of length  $L$ , the Coulomb interaction energy is roughly proportional to  $1/L$ , while the single particle confinement energy is roughly proportional to  $1/L^2$ . Therefore, the smaller the QD is, the smaller is the ratio between the two and the faster the calculations converge (less single particle states should be considered).

The FCI many-carrier Hamiltonian is written in second-quantization formalism [14], as

$$H = H_0 + H_{ee} + H_{hh} + H_{eh} \quad (1.2)$$

Where

$$\begin{aligned}
H_0 &= \sum_i \varepsilon_i^e a_i^\dagger a_i + \sum_j \varepsilon_j^h b_j^\dagger b_j \\
H_{ee} &= \frac{1}{2} \sum_{i_1, i_2, i_3, i_4} C_{i_1, i_2, i_3, i_4}^{eeee} a_{i_1}^\dagger a_{i_2}^\dagger a_{i_3} a_{i_4} \\
H_{hh} &= \frac{1}{2} \sum_{j_1, j_2, j_3, j_4} C_{j_1, j_2, j_3, j_4}^{hhhh} b_{j_1}^\dagger b_{j_2}^\dagger b_{j_3} b_{j_4} \\
H_{eh} &= \sum_{i_1, j_2, j_3, i_4} \left( -C_{i_1, j_2, j_3, i_4}^{ehhe} + C_{j_2, i_1, j_3, i_4}^{hehe} \right) a_{i_1}^\dagger b_{j_2}^\dagger b_{j_3} a_{i_4}
\end{aligned} \tag{1.3}$$

$H_0$  is the single particle Hamiltonian, presumed to be already diagonalized, where  $\varepsilon_i^e$  ( $\varepsilon_j^h$ ) is the energy of the single electron (hole) state number  $i$  ( $j$ ).  $H_{ee}$  ( $H_{hh}$ ,  $H_{eh}$ ) is the electron-electron (hole-hole, electron-hole) interaction Hamiltonian. The operator  $a_i^\dagger$  ( $b_j$ ) creates (annihilates) an electron (a hole) in the single-electron (hole) state number  $i$  ( $j$ ). The electron and hole creation and annihilation operators have the usual Fermionic *anti*-commutation relations. This ensures the anti-symmetry of the created states in the exchange of any pair of particles [14]. The second term in  $H_{eh}$  is the *electron-hole exchange interaction*. We show below that this term, which we add to our many-carriers' model for the first time [28] is the main source for linearly polarized spectral lines in the PL spectrum of single QDs.

Since it commutes with the electron number operator,  $N_e = \sum_i a_i^\dagger a_i$  and with the hole number operator,  $N_h = \sum_j b_j^\dagger b_j$  [14, 15], the Hamiltonian (1.3) can be written as a separate matrix for each number of electrons and holes. We do so by using the population basis. Each wavefunction in this basis represents a Slater determinant (a complete particle-exchange anti-symmetric state) composed of products of the chosen single carrier states. The Hamiltonian matrix is then diagonalized, and the many-body states and eigen-energies are obtained. Finally, the energies, the oscillator strengths and polarization selection rules for optical transitions between the

obtained many-body states are calculated using the dipole approximation.

In the following subsections, we discuss each step in the FCI model calculations.

### *Single carrier states*

There are various methods for calculating single carrier energies and states in semiconductor hetero-structures in general, and in QDs in particular [19-27]. These can be divided into two groups. The first group includes atomistic approaches, such as the pseudo-potential method [19] and the tight-binding method [20, 21]. The second group includes envelope function and effective mass approximations, such as single and multi-band k·P approximations [22-27] for the solution of the Schrödinger equation for a single carrier in the QD potential.

The methods in the first group consider the full atomic potential directly, and thus obtain the full wavefunctions in atomic resolution. They require the information about the type and position of every atom in the structure, and demand rather large amounts of computational resources.

In methods of the second group it is assumed that the wavefunctions can be written as a sum of products of an intra-unit-cell Bloch function,  $u_b(\vec{r})$ , periodic over all unit cells, and an inter-unit-cell envelope function,  $\phi_n^b(\vec{r})$ .

$$\psi_n = \sum_b \phi_n^b(\vec{r}) u_b(\vec{r}) \quad (1.4)$$

The summation is over all bands  $b$ . The problem is then reduced to finding the envelope functions, given the bulk material parameters (e.g. band-edge energies, carriers' dispersion functions, bulk elastic moduli, etc.) as a function of position. Without magnetic fields, Kramers theorem applies, and the bands are arranged in degenerate pairs [29]. Generally, every pair of degenerate states can be mapped onto a pair of spin 1/2 states, even if the real spin of the original states is not 1/2, or even not defined at all [14]. The new spin component associated with a state

is called the *pseudo-spin* component of the state. If only one (twice Kramers degenerate) band is considered, the equation for the envelope function reduces to a simple Schrödinger equation with an effective mass and an effective potential. For a zero magnetic field, this equation does not depend on the pseudo-spin of the state, and yields the same envelope wavefunction for each pseudo-spin component. Taking into account only one band is justified when the band in question is non-degenerate (except for the Kramers degeneracy) and energetically isolated from other bands. This is usually the case for an electron in the conduction band of wide band III-V semiconductors. The case of a hole in the valence band is more complicated. In these bulk materials the highest valence band states (the "heavy" and "light" hole states) are degenerate (at zero crystal momentum  $k=0$ ). In quantum structures, however, the confinement and the strain lift this degeneracy [23-25]. When this degeneracy removal is substantial, the single band description of the heavy hole band is still a good approximation.

Considering only a single band greatly reduces the amount of computational resources needed. It also offers direct intuitive insights into various model parameters and their influence on the calculated measurable properties of the QDs. It misses, though, some of the QD properties, notably properties which depend on orientation of the QD relative to the crystallographic axes of the semiconductor [28, 30]. These and other properties may require more complicated methods. However, due to the lack of structural information needed for these methods we prefer this approach and we shall use it throughout this chapter.

For the effective potential acting on the single band carrier we use a very simple model: A low constant potential inside a region in the shape of a rectangular or an elliptical slab, and a higher constant potential outside that region. These shapes belong to the  $D_{2h}$  symmetry group. The  $D_{2h}$  is the highest symmetry group without a 3-fold or higher symmetry axis. Higher symmetries

would not contain in-plane anisotropy, which is crucial for the appearance of linear polarizations in the PL emission. Lower symmetries would require a more complicated model for describing the QD potential, possibly with more free structural-parameters. Our model contains only three different geometrical parameters: the height, length and width of the lower potential volume. Due to the different band offsets and different strain effects, the potential for the hole has different parameters than that for the electron [25]. In an attempt to reduce the number of free parameters we express this freedom by only one additional parameter. Namely, the ratio between the length of the slab for the hole to that for the electron.

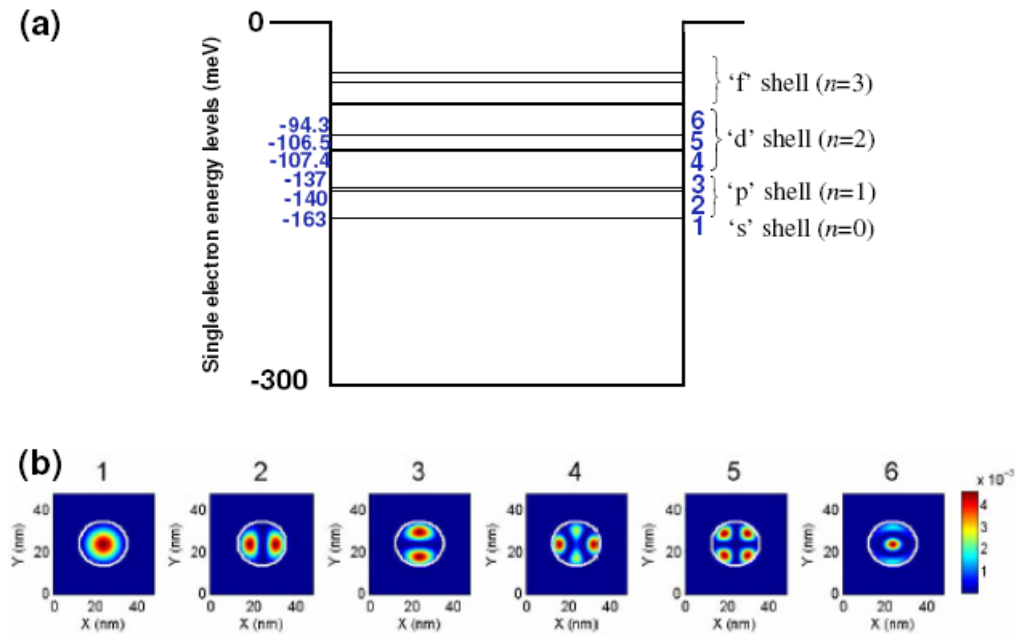


Fig. 3. (a) Single electron eigen-energies, numerically calculated for an elliptic slab model with height=3nm, length=23.2nm, width=21.2nm, and an electron effective mass of  $0.085m_0$ . (b) In-plane cross-sections of the calculated probability distributions (wavefunction squared) at half the slab's height.

For epitaxially grown, self-assembled QDs, the height (defined to be along the growth direction) is usually much smaller than the length and width [31]. The single particle wavefunctions are therefore quasi-two-dimensional, and have no nodes along the growth axis ( $z$ ). Each wavefunction can therefore be uniquely defined by two quantum numbers. These numbers,  $n_x$  and  $n_y$  respectively, reflect the number of the nodes in the carrier wavefunction along two axes perpendicular to the growth axis ( $n_z=0$ ). If the ratio between the width and length of the QD (the aspect ratio) is not far from 1 (a 'nearly symmetric' QD), all wavefunctions having the same total number of nodes,  $n=n_x+n_y$ , will have close energies, well separated from the energies of wavefunctions with different total number of nodes. The single particle spectrum is thus composed of 'shells'. Each shell contains  $2(n+1)$  states, where  $n$  is the total number of nodes ( $n=0,1,2,..$ ). The extra factor of 2 is due to the pseudo-spin (Kramers) degeneracy. As an example, Fig. 3 presents numerically calculated single-electron energies and wavefunctions for an elliptic slab. The model parameters were chosen to fit experimental measurements.

#### *Few carrier states – the role of the electron-hole exchange interaction*

The effects of the Coulomb interaction between the carriers, on the few-carrier energies and states can be quite generally divided into three types: Classical, Exchange and Correlation. In the classical picture, the few-particles states gain or lose energy due to the direct electrostatic interaction between their charge-densities. The interaction elements corresponding to this effect, the 'direct' Coulomb interactions -  $C_{i_1, i_2, j_2, j_1}^{eeee}$ ,  $C_{j_1, j_2, j_2, j_1}^{hhhh}$ ,  $C_{i_1, j_2, j_2, i_1}^{ehhe}$ , lie on the main diagonal of the Hamiltonian (1.2). Thus, they do not "mix" states of different symmetries and therefore do not have a direct effect on the form of the wavefunctions. The exchange Coulomb interaction elements result from the fact that in quantum mechanics, the carriers are indistinguishable. They

have the forms  $C_{i_2, i_1, i_2, i_1}^{eeee}$ ,  $C_{j_2, j_1, j_2, j_1}^{hhhh}$ ,  $C_{j_2, i_1, j_2, i_1}^{hehe}$ . Elements of this type can be off-diagonal, but then they connect only wavefunctions which have the *same* diagonal element (including the classical Coulomb terms) [14]. Thus, they can be viewed as first-order perturbations within degenerate subspaces. The form of the eigen-wavefunctions within each degenerate subspace is determined by the diagonalization of the exchange interaction in that subspace. These 'first-order' few-particles wavefunctions, which still contain a well defined spatial wavefunction for each particle, are called 'configurations' (due to sub-space diagonalization, the pseudo-spin is often ill-defined for each single carrier separately). Correlation Coulomb interaction elements are all the elements which are neither classical nor exchange. They are all off-diagonal, and connect different degenerate subspaces. Thereby, they mix states of different configurations. The inclusion of such elements in the calculation is the source of the name 'configuration-interaction'. The influence of each type of interaction elements is illustrated in Fig. 4.

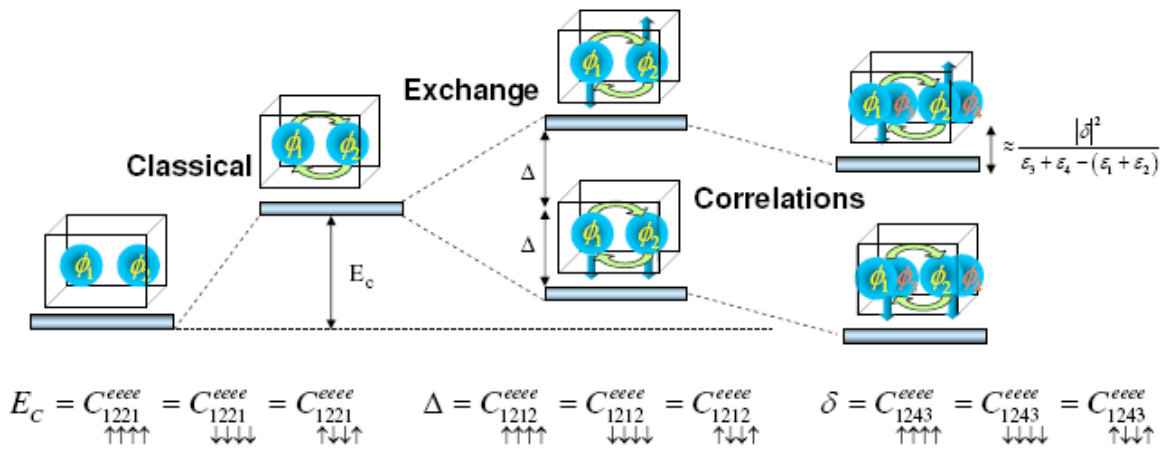


Fig. 4. Schematic description of the three type of coulomb interactions between two confined charge carriers and their effect on the mutual two carriers wavefunction and energy. Circles represent spatial single carrier wavefunctions. Arrows represent single carriers' pseudo-spins. The wavefunction indices were separated into spatial (1,2,...) and pseudo-spin ( $\uparrow, \downarrow$ ) components.

In order to calculate the Coulomb interaction elements, Eq. (1.1), in the envelope function approximation (Eq. (1.4)), it is convenient to separate the integration over the entire crystal into integration within a unit cell (of volume  $\Omega$ , centered at the lattice vector  $\vec{R}$ ), and summation over all unit cells:

$$\int d^3r = \sum_{\vec{R}} \int_{\Omega_{\vec{R}}} d^3r \quad (1.5)$$

When the potential varies slowly over the length of one unit cell, it follows that the envelope function of the confined carrier varies slowly on that length scale as well. It could therefore be considered constant over the volume of one unit cell. This approximation is the slowly-varying envelope function approximation (SVEFA). If only one (Kramers degenerate) band is included for each type of particle (band mixing is neglected), and the SVEFA is used, the integral (1.1) becomes,

$$C_{\substack{n_1, n_2, n_3, n_4 \\ s_1, s_2, s_3, s_4}}^{p_1 p_2 p_3 p_4} = \sum_{\vec{R}_1, \vec{R}_2} \phi_{n_1}^{p_1*}(\vec{R}_1) \phi_{n_2}^{p_2*}(\vec{R}_2) \phi_{n_3}^{p_3}(\vec{R}_2) \phi_{n_4}^{p_4}(\vec{R}_1) \times \\ \times \iint_{\Omega} \frac{e^2}{\epsilon |\vec{R}_1 - \vec{R}_2 + \vec{l}_1 - \vec{l}_2|} u_{p_1, s_1}^*(\vec{l}_1) u_{p_2, s_2}^*(\vec{l}_2) u_{p_3, s_3}(\vec{l}_2) u_{p_4, s_4}(\vec{l}_1) d^3l_1 d^3l_2 \quad (1.6)$$

where we have defined  $\vec{r} = \vec{R} + \vec{l}$ ,  $\vec{R}$  being the lattice vector closest to  $\vec{r}$ , and the Bloch amplitudes' periodicity was used. We would now like to obtain the  $\vec{R}$  dependence of the intra-unit cell integral of Eq. (1.6). For this purpose, the Coulomb operator is decomposed into a sum of products of a function of  $\vec{R}_1 - \vec{R}_2$  and a function of  $\vec{l}_1 - \vec{l}_2$ . This is done by dividing the integration space into two sub spaces: the *long-range* subspace, where  $\vec{R}_1 - \vec{R}_2 > \vec{l}_1 - \vec{l}_2$ , and the *short-range* subspace, where  $\vec{R}_1 - \vec{R}_2 < \vec{l}_1 - \vec{l}_2$ .

For the short range subspace, since  $\vec{l}_1$  and  $\vec{l}_2$  are intra-unit-cell vectors, in most cases  $\vec{R}_1 = \vec{R}_2$ ,

and one can make the approximation,

$$\frac{1}{|\vec{R}_1 - \vec{R}_2 + \vec{l}_1 - \vec{l}_2|} \cong \frac{1}{|\vec{l}_1 - \vec{l}_2|} v_0 \delta(\vec{R}_1 - \vec{R}_2)$$

where  $v_0$  is the volume of a unit cell.

For the long-range subspace, the Coulomb interaction operator can be expanded into a Taylor ('multi-pole') series,

$$\begin{aligned} \frac{1}{|\vec{R}_1 - \vec{R}_2 + \vec{l}_1 - \vec{l}_2|} &\cong \frac{1}{|\vec{R}_1 - \vec{R}_2|} - \frac{(\vec{R}_1 - \vec{R}_2)^T}{|\vec{R}_1 - \vec{R}_2|^3} \cdot (\vec{l}_1 - \vec{l}_2) \\ &+ \frac{1}{2} (\vec{l}_1 - \vec{l}_2)^T \cdot \frac{3(\vec{R}_1 - \vec{R}_2)(\vec{R}_1 - \vec{R}_2)^T - I}{|\vec{R}_1 - \vec{R}_2|^5} \cdot (\vec{l}_1 - \vec{l}_2) + \dots \end{aligned} \quad (1.7)$$

where  $I$  is the 3x3 identity matrix.

The intra-unit-cell integration can now be performed independently for each element (of both the short- and long-range subspaces), yielding functions of known dependence of  $\vec{R}_1$  and  $\vec{R}_2$ . Under the SVEFA the summation over  $\vec{R}_1$  and  $\vec{R}_2$  can be replaced by an integral over the entire space, and it can be assumed that  $\vec{R} \cong \vec{r}$ . The Coulomb integrals thus have the general form,

$$C_{\substack{n_1, n_2, n_3, n_4 \\ s_1, s_2, s_3, s_4}}^{p_1 p_2 p_3 p_4} = \sum_m \iint d^3 r_1 d^3 r_2 \phi_{n_1}^{p_1*}(\vec{r}_1) \phi_{n_2}^{p_2*}(\vec{r}_2) \hat{C}_{\substack{s_1, s_2, s_3, s_4 \\ p_1, p_2, p_3, p_4}}^{(m)}(\vec{r}_1 - \vec{r}_2) \phi_{n_3}^{p_3}(\vec{r}_2) \phi_{n_4}^{p_4}(\vec{r}_1) \quad (1.8)$$

where  $m$  counts the orders of the long-range expansion and also the short-range term, and

$\hat{C}_{\substack{s_1, s_2, s_3, s_4 \\ p_1, p_2, p_3, p_4}}^{(m)}(\vec{r}_1 - \vec{r}_2)$  represents the operator in inter-unit-cell space remaining after the intra-unit-

cell integral has been performed. This operator depends on  $s_{1..4}$  - the pseudo-spin components,

and on  $p_{1..4}$  - the particle identifiers, which together uniquely identify the Bloch amplitudes of

the participating single carrier wavefunctions (see Eq. (1.6)). Other than the operator, the integral

contains only single carrier envelope functions, numbered by their own separate indices,  $n_{1..4}$ .

Except for the case of the electron-hole-exchange interaction (EHEI), the zeroth order of the multi-pole series, Eq. (1.7), (the monopole-monopole term), when integrated, is much larger than all the other orders, including the short range term [15]. In such cases, to first

approximation, one can keep only this order. The operator  $\hat{C}_{\substack{s_1, s_2, s_3, s_4 \\ p_1, p_2, p_3, p_4}}^{(0)}(\vec{r}_1 - \vec{r}_2)$  for the monopole-monopole long-range interaction is given by

$$\hat{C}_{\substack{s_1, s_2, s_3, s_4 \\ p_1, p_2, p_3, p_4}}^{(0)}(\vec{r}_1 - \vec{r}_2) = \delta_{p_1, p_4} \delta_{p_2, p_3} \delta_{s_1, s_4} \delta_{s_2, s_3} \frac{e^2}{\epsilon |\vec{r}_1 - \vec{r}_2|} \quad (1.9)$$

This term gives rise to the well known same-carrier isotropic (Hisenberg-type) exchange interaction, which arranges the states according to their total pseudo-spin (separately for each type of carrier). For example, it divides the four-fold degenerate subspace of two identical carriers occupying two different spatial orbitals into a pseudo-spin-zero singlet and a pseudo-spin-one triplet (as schematically shown in Fig. 4). In this approximation, this interaction is not sensitive to the anisotropy in the potential shape. This is, however, not the case for the EHEI, since for it the operator in Eq. (1.9) strictly vanishes. Thus, for the EHEI, the leading term includes a short-range term, and the long-range dipole-dipole term (the monopole-dipole terms contribute only to correlation integrals and only when band mixing is not neglected). The short range EHEI operator reads [17],

$$\hat{C}_{\substack{s_1, s_2, s_3, s_4 \\ h, e, h, e}}^{(short)}(\vec{r}_1 - \vec{r}_2) = v_0 E_{SR} \delta_{s_1, s_4} \delta_{s_2, s_3} \delta_{s_1, s_3} \delta(\vec{r}_1 - \vec{r}_2) \quad (1.10)$$

where  $v_0$  is the volume of one unit-cell, and  $E_{SR}$  is the following intra-unit-cell integral:

$$E_{SR} = \int_{\Omega} d^3 l_1 d^3 l_2 u_{h,s}^*(\vec{l}_1) u_{e,s}^*(\vec{l}_2) \frac{e^2}{\epsilon |\vec{l}_1 - \vec{l}_2|} u_{h,s}(\vec{l}_2) u_{e,s}(\vec{l}_1). \quad (1.11)$$

The operator (1.10) is an isotropic contact interaction between an electron and a hole. The term differentiates in energy between a state in which the electron and the hole have parallel pseudo-spins and that in which their pseudo-spins are anti-parallel.

The EHEI long-range dipole-dipole operator reads [17],

$$\hat{C}_{h,e,h,e}^{(2),s_1,s_2,s_3,s_4}(\vec{r}_1 - \vec{r}_2) = \vec{\mu}_{s_1,s_2}^\dagger \frac{e^2 (I - 3\vec{n}\vec{n}^\dagger)}{\varepsilon |\vec{r}_1 - \vec{r}_2|^3} \vec{\mu}_{s_3,s_4} \quad (1.12)$$

where  $I$  is the 3x3 identity matrix,  $\vec{n} = (\vec{r}_1 - \vec{r}_2)/|\vec{r}_1 - \vec{r}_2|$ , and  $\vec{\mu}_{s,s'} = \int_{\Omega} d^3l u_{h,s}^*(\vec{l}) \vec{l} u_{e,s'}(\vec{l})$ .

From symmetry considerations it can be shown that [17]

$$\vec{\mu}_{\uparrow,\downarrow}^\dagger = \mu(\hat{x} - i\hat{y}); \quad \vec{\mu}_{\downarrow,\uparrow}^\dagger = \mu(\hat{x} + i\hat{y}); \quad \vec{\mu}_{\uparrow,\uparrow}^\dagger = \vec{\mu}_{\downarrow,\downarrow}^\dagger = 0. \quad (1.13)$$

Here  $\uparrow$  ( $\downarrow$ ) represents an electron (hole) pseudo-spin  $+\frac{1}{2}$  [32]. Using Bloch amplitudes at  $k=0$  and the connection between the position and momentum expectation values [33], the value  $\mu^2$  can be estimated as [28],

$$\mu^2 \cong \frac{\hbar^2 E_p}{4m_0 E_G^2} \quad (1.14)$$

where  $E_p$  is the conduction-valence band-interaction energy [25],  $E_G$  is the band-gap, and  $m_0$  is the mass of a free-electron.

When the operator (1.12) acts on the envelope functions, it resembles a quadruple interaction. As such it vanishes completely if the QD has in-plane rotational symmetry which is larger than two folds. Therefore, this interaction is the main mechanism which leads to the appearance of linearly polarized emission lines in the PL spectrum of self-assembled QDs.

The leading terms in the EHEI interaction can thus be cast into an interaction Hamiltonian of the following form:

$$H_{EHEI} = \sum_{\substack{n_1, n_2, n_3, n_4 \\ s_1, s_2, s_3, s_4}} C_{n_1, n_2, n_3, n_4, s_1, s_2, s_3, s_4}^{hehe} a_{n_1, s_1}^\dagger b_{n_2, s_2}^\dagger b_{n_3, s_3} a_{n_4, s_4} \quad (1.15)$$

For each combination  $n_1..n_4$  of envelope functions, using (1.10), (1.12) and (1.13), the elements

$C_{n_1, n_2, n_3, n_4, s_1, s_2, s_3, s_4}^{hehe}$  can be arranged into the following 4x4 matrix in the electron-hole pseudo-spin basis,

$s_2 s_1, s_4 s_3 \in \{\downarrow\uparrow, \uparrow\downarrow, \uparrow\uparrow, \downarrow\downarrow\}$  [17]:

$$C_{n_1, n_2, n_3, n_4, s_1, s_2, s_3, s_4}^{hehe} = \begin{pmatrix} \Delta_0^{n_1, n_2, n_3, n_4} & \frac{1}{2} \Delta_1^{n_1, n_2, n_3, n_4} & 0 & 0 \\ \frac{1}{2} \Delta_1^{n_1, n_2, n_3, n_4*} & \Delta_0^{n_1, n_2, n_3, n_4} & 0 & 0 \\ 0 & 0 & 0 & \frac{1}{2} \Delta_2^{n_1, n_2, n_3, n_4} \\ 0 & 0 & \frac{1}{2} \Delta_2^{n_1, n_2, n_3, n_4*} & 0 \end{pmatrix} \quad (1.16)$$

This matrix represents also the electron-hole-exchange Hamiltonian for the more familiar case of one electron and one hole [18] which is obtained from (1.16) by the subtraction of

$\frac{1}{2} \Delta_0^{n_1, n_2, n_3, n_4}$  from the main diagonal.

The terms  $\Delta_0^{n_1, n_2, n_3, n_4}$  are often called the 'isotropic electron-hole exchange'. They are not sensitive to in-plane anisotropy, and separate only states with parallel pseudo-spins from those with anti-parallel pseudo-spins. They contain the short-range interaction and the 'out-of plane' component of the long range interaction:

$$\Delta_0^{n_1, n_2, n_3, n_4} = v_0 E_{SR} \int d^3 r \phi_{n_1}^{h*}(\vec{r}) \phi_{n_2}^{e*}(\vec{r}) \phi_{n_3}^h(\vec{r}) \phi_{n_4}^e(\vec{r}) + \frac{e^2 \mu^2}{\epsilon} \iint d^3 r_1 d^3 r_2 \phi_{n_1}^{h*}(\vec{r}_1) \phi_{n_2}^{e*}(\vec{r}_2) \frac{2n_z^2 - n_x^2 - n_y^2}{|\vec{r}_1 - \vec{r}_2|^3} \phi_{n_3}^h(\vec{r}_2) \phi_{n_4}^e(\vec{r}_1) \quad (1.17)$$

Where  $v_0$  and  $E_{SR}$  are defined in (1.11),  $\vec{n}$  is defined in (1.12), and  $\mu$  is defined in (1.13).

The terms  $\Delta_2^{n_1, n_2, n_3, n_4}$  split the states  $\uparrow\uparrow, \downarrow\downarrow$ . In the single-band approximation, this term vanishes [17]. However, from symmetry considerations it appears that for zincblende crystals of symmetry which is lower than that of a sphere [16] it should not vanish. These terms result from

the isotropic EHEI when band-mixing is considered. These terms do not have impact on the polarization selection rules and are generally quite small in respect to the other terms in (1.16) [34]. We set them to zero (unless stated otherwise) in the discussion that follows.

The terms  $\Delta_1^{l_1, l_2, l_3, l_4}$  are called the 'anisotropic electron-hole exchange interaction' [16-18].

In the single-band approximation they are pure long-range, and are given by,

$$\frac{1}{2} \Delta_1^{l_1, l_2, l_3, l_4} = \frac{3e^2 \mu^2}{\epsilon} \iint d^3 r_1 d^3 r_2 \phi_{l_1}^{h*}(\vec{r}_1) \phi_{l_2}^{e*}(\vec{r}_2) \frac{n_y^2 - n_x^2 + 2in_x n_y}{|\vec{r}_1 - \vec{r}_2|^3} \phi_{l_3}^h(\vec{r}_2) \phi_{l_4}^e(\vec{r}_1) \quad (1.18)$$

For electron and hole in their lowest single particle state, the anisotropic electron-hole exchange interaction removes the degeneracy between the states  $\downarrow\uparrow, \uparrow\downarrow$  by  $|\Delta_1^{1,1,1,1}|$ . The resulting eigenstates are  $(\downarrow\uparrow \pm e^{i2\phi} \uparrow\downarrow) / \sqrt{2}$  ('+' for the lower energy). Here  $\phi$  is defined as the angle between the major axis of the QD and the x axis of the frame of reference. Thus,

$\Delta_1^{1,1,1,1} \equiv -|\Delta_1^{1,1,1,1}| e^{i2\phi}$ . Obviously, by a proper choice of the coordinates  $\phi$  can be set to 0. As we show below, optical transitions to and from these states are cross linearly polarized.

The integrals (1.18) can be numerically calculated if the single-carrier envelope wavefunctions are accurately known [17]. In order to get insight and to save computational resources we obtained approximate analytical model for these calculations. First, since lattice mismatch strain induced QDs are typically quite flat and their dimension along the growth direction is order of magnitude smaller than their lateral extent, we use a 2D model for describing the QD potential. The integrals' dimensionality is thus reduced to four. We then approximate the QD potential by a parabolic expression and obtain analytical wavefunctions for the single charge carriers [26-28]. With these wavefunctions, three of the four integrations can be analytically obtained. The last integral can then be easily calculated numerically. For a nearly round QD, even this integral can

be obtained analytically by expanding it into a power series in the aspect ratio of the model QD, and then keeping terms up to first order only. The result of this derivation for  $\Delta_1^{1,1,1,1}$  is,

$$\Delta_1^{1,1,1,1} \cong \frac{3\sqrt{\pi}e^2\mu^2(\xi-1)}{2\varepsilon\beta\sqrt{1+\beta^2}(l_x^e)^3\xi^2} \quad (1.19)$$

where  $\mu^2$  is given by Eq. (1.14),  $l_x^e$  is the characteristic length (semi-axis) of the electron Gaussian wave function in the x direction,  $\beta$  is the ratio between the characteristic length of the hole wave function to that of the electron, and  $\xi$  is the length ratio between the minor and major axes of the QD – namely its aspect ratio. We chose the x-axis to be along the long axis of the QD thereby setting  $\phi$  to zero. For  $\xi = 0.96$ ,  $\beta = 0.72$ , and  $l_x^e = 72\text{\AA}$  [28] which result in fairly good agreement between the calculated PL spectra and the measured one, Eq. (1.19) yields  $\Delta_1^{1,1,1,1} = 15\mu\text{eV}$ , not too far from the measured value of  $30\mu\text{eV}$  [7]. All the other  $\Delta_1^{l_1,l_2,l_3,l_4}$  terms can be similarly obtained. Some examples for these terms are given in Table 1.

Table 1. Ratios of a few anisotropic electron-hole exchange terms to the term of a ground-state exciton, for a nearly symmetric QD ( $|\xi - 1| \ll 1$ ). The values given in the third column are for the case where  $\xi = 0.96$  and  $\beta = 0.72$ .

Electron-hole exchange term	Ratio to $\Delta_1^{1,1,1}$	Value of the ratio to $\Delta_1^{1,1,1}$
$\Delta_1^{1,2,1,2}$	$\frac{\beta^2}{1 + \beta^2} \frac{2\xi - 1}{\xi - 1}$	-7.84
$\Delta_1^{2,1,2,1}$	$\frac{1}{1 + \beta^2} \frac{2\xi - 1}{\xi - 1}$	-15.16
$\Delta_1^{1,3,1,3}$	$\frac{\beta^2}{1 + \beta^2} \frac{\xi - 2}{\xi - 1}$	+8.88
$\Delta_1^{1,2,1,3}$	$i \frac{\beta^2}{1 + \beta^2} \frac{\xi + 1}{2(\xi - 1)}$	-8.36 <i>i</i>
$\Delta_1^{1,4,1,4}$	$\frac{\beta^4}{(1 + \beta^2)^2} \frac{41 - 6\xi}{16}$	+0.256
$\Delta_1^{2,2,2,2}$	$\frac{\beta^2}{(1 + \beta^2)^2} \frac{61\xi - 45}{16(\xi - 1)}$	-4.76

### *Optical transitions between the states and polarization selection rules*

Once the many carrier states are known, optical transitions between these states can be quite accurately and straight forwardly calculated using the dipole approximation. The dipole operator can be expressed as [13]

$$\hat{P} = \sum_{ij} \bar{p}_{ij} a_i b_j \quad (1.20)$$

In the single-band SVEFA, the inter-band transition momentum vector  $\bar{p}_{ij}$  is given by

$$\bar{p}_{ij} \equiv \bar{p}_{l,l',s,s'} = \vec{M}_{s,s'} \int d^3 r \phi_l^{h*}(\vec{r}) \phi_{l'}^e(\vec{r}) \quad (1.21)$$

where the electron and heavy hole state indices (*i and j, respectively*) are explicitly expressed in

terms of their spatial ( $l, l'$ ) and pseudo-spin ( $s, s'$ ) components. For Bloch amplitudes at  $k=0$ , The momentum matrix elements  $\vec{M}_{s,s'}$  are given by

$$\vec{M}_{\uparrow,\downarrow}^\dagger = \frac{i}{2}\sqrt{m_0 E_p} (\hat{x} - i\hat{y}); \quad \vec{M}_{\downarrow,\uparrow}^\dagger = \frac{i}{2}\sqrt{m_0 E_p} (\hat{x} + i\hat{y}); \quad \vec{M}_{\uparrow,\uparrow}^\dagger = \vec{M}_{\downarrow,\downarrow}^\dagger = 0. \quad (1.22)$$

The recombination of an e-h pair with anti-parallel spins with hole spin  $\uparrow$  ( $\downarrow$ ) relative to the growth direction (z), therefore yields a right- (left-) hand circularly polarized photon (emitted in the z-direction). Thus, the recombination of an e-h pair (exciton) in a coherent state expressed as  $\alpha \uparrow\downarrow + \beta \downarrow\uparrow$  yields a photon of polarization  $\alpha\sigma^+ + \beta\sigma^-$ . In particular, if  $|\alpha| = |\beta|$ , the emitted photon will be linearly polarized in a direction which is rotated by an angle  $\phi = \frac{1}{2} \arg(\beta/\alpha)$  with respect to the x-axis. For  $|\alpha| \neq |\beta|$ , the polarization is elliptical. Exciton states with parallel electron and hole spins cannot recombine radiatively. Such states are called "dark excitons". The rate of optical transition at energy  $\varepsilon$  and polarization  $\vec{e}$ , is calculated using Fermi golden rule and the dipole approximation [35]:

$$\Gamma_{\vec{e}}(\varepsilon) = \frac{4\alpha n \varepsilon}{3\hbar m_0^2 c^2} \sum_{i,f} \left| \langle f | \vec{e} \cdot \hat{\vec{P}} | i \rangle \right|^2 \delta_{\varepsilon, \varepsilon_i - \varepsilon_f} F_i \quad (1.23)$$

where  $\alpha = \frac{e^2}{\hbar c} \cong \frac{1}{137}$  is the fine structure constant, and  $n$  is the refraction index of the QD

material. The indices  $i$  and  $f$  stand for initial and final state respectively and  $\varepsilon_i$  and  $\varepsilon_f$  are the energies of these states.  $F_i$  is the probability to find the system in the initial state  $i$ .

We now proceed to discuss some specific examples.

(a) *The neutral exciton:* As a simple example let us first examine the recombination of the ground bright neutral exciton ( $X^0$ ) states. These states are mainly composed of the configuration

of one electron and one hole in their respective lowest single carrier states. The EHEI results in four non-degenerate states. In the lowest energy pair of states, the electron and hole spins are parallel and the states are "dark". The highest energy pair of states (the "bright exciton") are:  $X_{H(V)}^0 = \frac{1}{\sqrt{2}}(\uparrow\downarrow \pm e^{i2\phi} \downarrow\uparrow)$ . They are separated in energy by  $|\Delta_1^{1,1,1}|$ . These states recombine radiatively by emitting cross linearly polarized photons and give rise to a doublet in the PL spectrum (See Fig. 5a). The lowest energy component of the doublet is polarized parallel to major axis of the QD and it is called "horizontal" (H). The highest one is polarized along the minor axis of the QD and is called "vertical" (V). Usually, the laboratory frame is chosen such that  $\phi = 0$ . In such a frame we calculate [28]:

$$\left| \left\langle 0 \left| \hat{x} \cdot \hat{P} \right| X_H^0 \right\rangle \right|^2 = \left| \left\langle 0 \left| \hat{y} \cdot \hat{P} \right| X_V^0 \right\rangle \right|^2 = 1.44 \times \frac{m_0 E_P}{2} \quad (1.24)$$

The factor 1.44 is due to the contributions of other spatial configurations to the ground-state wavefunction. Assuming equal population probabilities for the two bright  $X^0$  states, and the two dark  $X^0$  states, we obtain a total bright  $X^0$  rate of  $(0.8 \text{ ns})^{-1}$ , in excellent agreement with the measured lifetime [7].

The calculated rates of all other optical transitions presented below, are given in units of this rate.

We now proceed to examine a few other examples.

*(b) Neutral biexciton recombination:* A neutral biexciton ( $XX^0$ ) consists of two electrons and two holes. Its ground state is mostly composed of the configuration where all carriers are in their lowest single-carrier level. Since there are two carriers in each spatial state, due to Pauli's exclusion principle, the state must be anti-symmetric under spin exchange – a spin-singlet state. Due mostly to the Coulomb correlation [36], the energy difference between the  $XX^0$  and the  $X^0$  states is different than that between the  $X^0$  states and the 0 (empty QD – "vacuum") state. This

leads to a difference in the recombination energies between the  $X^0$  and the  $XX^0$ . This difference, mostly referred to as the "biexciton binding energy", is usually on the order of a few meV, and it can be either positive or negative [36]. Like in the  $X^0$  transition, the  $XX^0$  transition includes cross-linearly polarized doublet. The doublet originates from the exciton states as well. Therefore the  $XX^0$  splittings is the same as that of the  $X^0$ . But, since in the biexciton transition the exciton is the final state, the energy order of the doublet's components is opposite to that of the exciton (Fig 5a).

*(c) Singly charged excitons:* If the QD contains an additional electron (hole) along-side the exciton, the combined state is called a singly negatively (positively) charged exciton, or a negative (positive) trion. We mark the relevant state as  $X^{-1}$  ( $X^{+1}$ ). In its ground state the three carriers are mostly in their respective lowest energy state. Due to Pauli's principle, the two carriers of same sign are in a spin-singlet state. The unpaired, minority carrier, can be in one of two possible spin states. Due to Kramers theorem [29], in the absence of magnetic field these states are degenerate.

Upon recombination, one majority carrier is left in the QD. It, too, has two Kramers degenerate spin states. The selection rules for optical recombination (1.22) permit only two optical transitions between the trion and the charged state. These two transitions are in opposite polarizations. Thus, in the PL spectrum, only one, unpolarized PL line is expected for each charged exciton (Fig. 5b). Applying external magnetic field, which lifts the degeneracy, results (in Faraday configuration) in a cross-circularly, polarized doublet [18].

*(d) Singly charged biexcitons:* The main configuration consists of two electrons and two heavy-holes in their lowest single carrier level, and an additional charge in its second single carrier level. We mark these charged biexcitons as  $XX^{+1}$  or  $XX^{-1}$  for positive or negative extra charge,

respectively. Like the case of the charged exciton, Kramers degeneracy holds here as well. Due to the small spatial overlap between the wavefunctions of charge carriers of different orbitals, radiative recombination of such e-h pairs is weak [see Eq. (1.21)]. Therefore, we consider only recombinations between e-h pairs in their lowest levels. When such recombination occurs, the QD is left in an excited charged exciton state, with one of the majority carriers in its second orbital level (see Fig. 5c). Since there are 3 unpaired carriers now, there are 8 possible spin configurations. The strongest exchange interaction within this subspace is the same-particle exchange. It divides the 8 states into two groups by the total spin of the two same-charge carriers. The high energy group consists of the states where the same-charge carriers form a spin-zero singlet (anti-symmetric under same carrier exchange) state and in the low energy group they form triplet (symmetric under same carrier exchange) spin states. We name the high energy group S and the low energy group T.

The spin of the minority carrier in each of these groups can be oriented either up or down. The electron-hole exchange interaction (EHEI) between this carrier and the other two defines the energy of the configuration. Among the S states, in both cases, the spin of the minority carrier is parallel to one of the majority carriers and anti-parallel to the other one. Thus the S group remains doubly (Kramers) degenerate. Among the T states there are three possible configurations, resulting in three different energies. The lowest energy is the one in which all three spins are oriented along the same direction. The highest energy is the one in which the minority carrier is anti-parallel to both majority carrier spins. The one in between is the case in which it is parallel to one and anti parallel to the other (see Fig. 5c).

It is easy to see that the lowest level, in which all the spins are parallel, cannot be reached by radiative annihilation of an e-h pair from the charged biexciton state. Therefore, the

recombination of the charged biexciton results in three spectral lines: a single, low energy line, which lead to the high energy S level, and two higher energy lines which lead to the two accessible T levels (Fig. 5c). We mark these optical transitions by S,  $T_0$  and  $T_1$  ( $T_3$ ), to associate the subscript with the total spin projection of the two electrons (heavy-holes) majority carriers. We note that the S and  $T_0$  lines have half the oscillator strength of the  $T_1$  (or  $T_3$ ) line, since only half of their wavefunctions is reached by annihilating e-h pair from the charged biexciton state (see Fig 5c).

In the absence of additional interactions, these lines should be unpolarized. This is because each level is doubly (Kramers) degenerate and two orthogonally polarized transitions between the levels are equally probable.

The anisotropic EHEI becomes important when the symmetry of the QD reduces. Due to its form (1.16) it mixes only states where there are antiparallel e-h spin components (assuming  $\Delta_2$  is negligible [34]). This mixing results in photon emission which reflects the reduced symmetry of the system, i.e. with *linear* polarization components testifying to the preferred directionality of the system. The degree of linear polarization reflects the magnitude of the level mixing term (the anisotropic EHEI), relative to the levels separation. Therefore, while the mixing between the  $T_0$  and the  $T_{1(3)}$  results in partial orthogonal linear polarizations, the S level remains essentially unpolarized. A more detailed quantitative description of this dependence can be found in refs. 37 and 38.

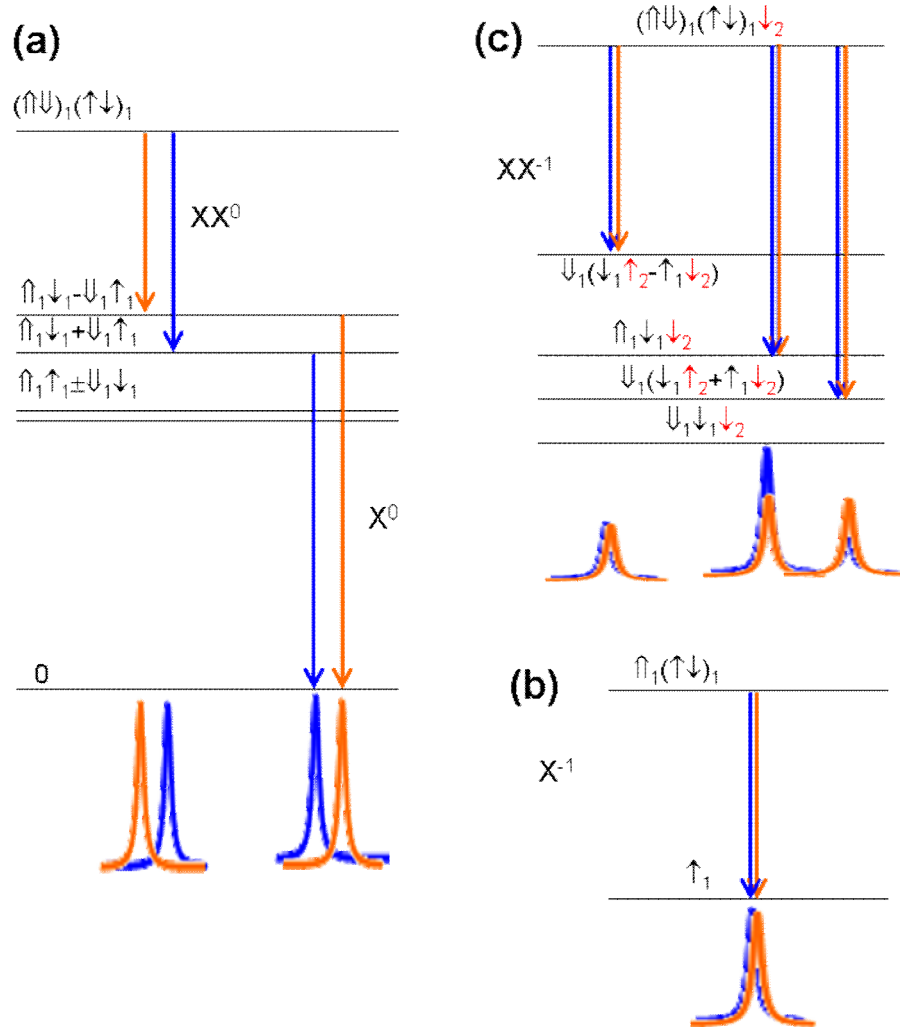


Fig. 5: Schematic description of energy levels and inter-level optical transitions. (a) Neutral exciton ( $X^0$ ) and biexciton ( $XX^0$ ), (b) negatively charged exciton ( $X^{-1}$ ) and (c) negatively charged biexciton ( $XX^{-1}$ ). The most significant electronic configuration is described above each level. In (b) and (c) only one of the two Kramers degenerate states is described. Thin (thick) arrows represent electron (heavy hole) pseudo-spin (see text). The subscript numbers represent the orbital part of the single carrier wavefunction (see Fig. 3). Note that the presented wavefunctions are not-normalized. Below each transition diagram, a schematic polarization sensitive PL spectrum is presented. Light (dark) gray line shows the spectrum in horizontal (vertical) polarizations.

(e) *Doubly negatively charged exciton*: The main ground state configuration of a doubly negatively charged exciton consists of two paired electrons in the lowest single electron state, a hole in the lowest hole state, and an additional electron in the second electron state. The two paired electrons have spin zero, and are exchange-inert. The remaining is an e-h pair, where the hole is in its lowest state and the electron is in its second state. There are four spin configurations, similar to those of the neutral exciton. The main difference is in the actual value of the anisotropic EHEI which, as can be seen in Table 1, is larger in its absolute value than that of ground-state neutral exciton, and opposite in sign to it. After recombination of a ground level e-h pair, the QD is left with two electrons, in different orbital states. The final states are therefore divided into a high energy electronic singlet and low energy electronic triplet. These states are energetically separated by the same-charge (elect.-elect.) exchange interaction. While the triplet states can be reached from all four initial states, the singlet state can be reached only from the two states where the unpaired electron and hole's spins are anti-parallel. Therefore, there are two groups of spectral lines: A low-energy cross-linearly polarized doublet, and a high energy triplet, made of a higher energy cross-linearly polarized doublet and a lower energy, unpolarized single line (or more accurately a degenerate doublet). We note that within each doublet the two cross-linearly polarized components appear in opposite energy order. This is a consequence of the difference in the symmetry under spin-exchange between the final states in each case (Fig. 6a).

(f) *Triply negatively charged exciton*: This configuration contains one hole and four electrons confined in the QD. There are two possibilities for the configuration of the lowest energy state. If the energy difference between the second and third single electron levels is larger than the electron-electron exchange interaction between these levels,  $C_{\uparrow,\uparrow,\uparrow,\uparrow}^{eee}$ , than the electronic spin configuration would be of two closed shells. In this case the total electronic spin is zero (Fig. 6b).

In the opposite case, the two higher energy electrons would prefer to be in open shells, forming spin triplet configuration thereby reducing the level energy by the electron-electron exchange energy (see Fig. 6c). As shown in the figure, for the closed shell case, both initial and final states are doubly degenerate, giving rise to a single, unpolarized spectral line (like in the case of the ground state singly charged exciton). For the open shell case, the situation is markedly different, yielding a much richer spectrum. The initial states resemble the final states of the singly charged biexciton. They are arranged in three levels with a Kramers' degenerate pair of states in each level. All the states are optically active. The final states are those of three electrons, each in its own spatial state. As shown in Fig. 6c, the 8 spin configurations are divided by the electron-electron exchange interaction according to their total spin to a lower energy quadruplet (total spin  $3/2$ ), and two higher energy doublets (total spin  $1/2$ ). The quadruplet can be reached optically from all three levels of the initial configuration. The higher doublet can be reached only from the two higher energy levels of the initial state. The intermediate level cannot be reached from any one of the three initial levels. This gives rise to two groups of spectral lines, a higher energy group consisting of three lines, and a lower energy group consisting of two lines (Fig. 6c). Considering the different spin configurations involved in each the transitions, it can be shown [39] that the intensity ratio between the lines in the group of three is 3:2:1 (from lowest to highest energy), and 2:1 in the group of two lines.

Similar to the radiative decay of the singly charged biexciton, the two higher energy initial states of the open shells triply charged exciton are mixed by the anisotropic EHEI. This leads to partial linear polarizations in the spectral lines resulting from their recombinations. As we show below, our experimentally measured polarization sensitive PL spectra is compatible with the second case: The triply negatively charged exciton is best described by the open-shells configuration.

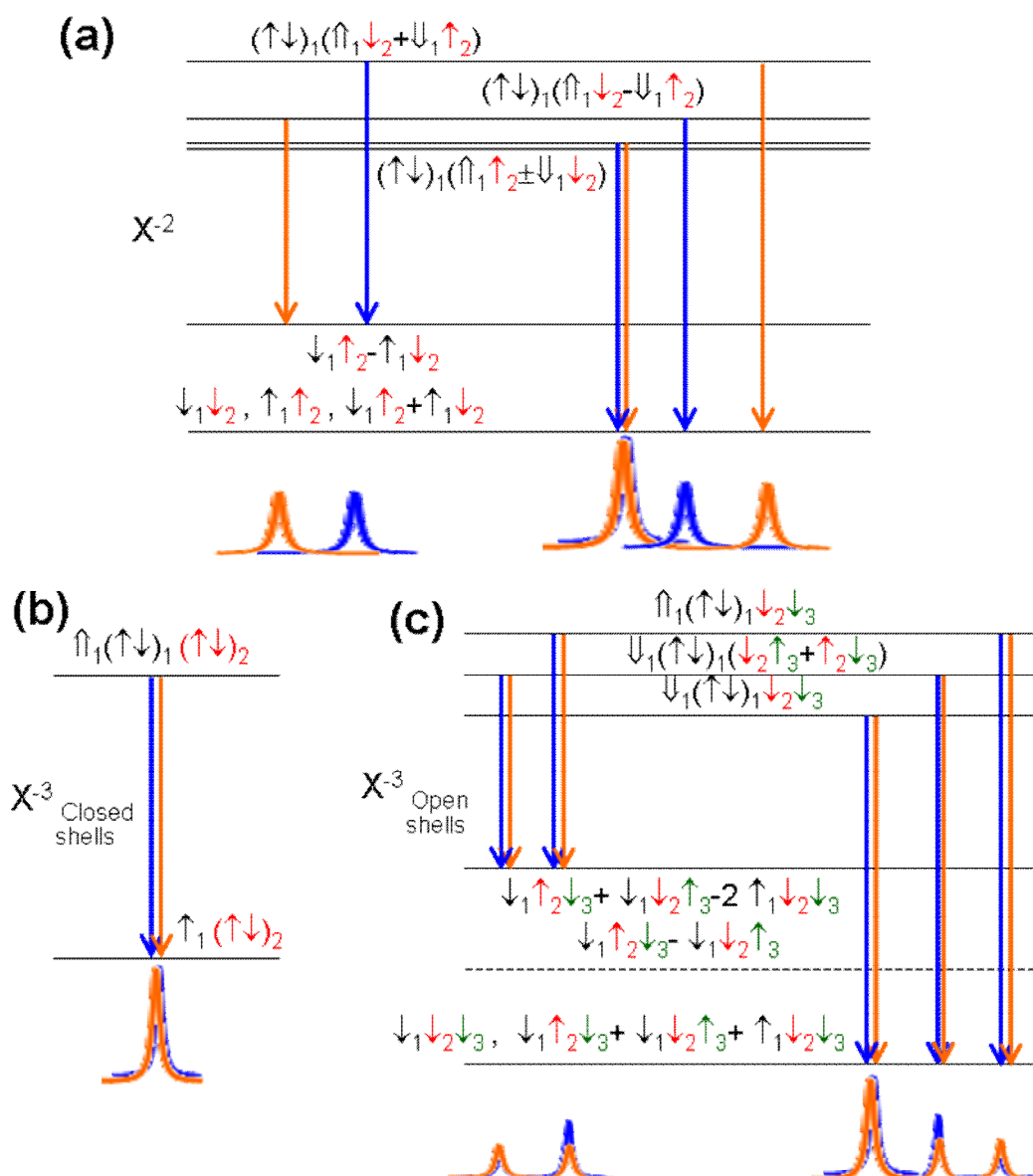


Fig. 6. Schematic description of energy levels and inter-level optical transitions: (a) Doubly negatively charged exciton ( $X^{-2}$ ), (b) triply negatively charged exciton ( $X^{-3}$ ) in closed-shells configuration, and (c)  $X^{-3}$  in open shells configuration. The most significant electronic configuration is given above each level. The notations are explained in Fig. 5. In (b) and (c) only one of the two Kramers degenerate states is given for each level. Below each transition diagram, a schematic polarization sensitive PL spectrum is presented.

### *Polarization sensitive photoluminescence spectrum*

In this section we present measured polarization sensitive PL spectra and compare the details of the spectral lines observed with the model calculated transitions. This comparison, together with polarization memory measurements [40] and external field dependent PL measurements [28], are used for the identification of the spectral lines.

The sample used for the experiments presented here contains a single layer of In(Ga)As QDs embedded within a GaAs matrix. The QD layer was positioned at the middle of a one-wavelength cavity, made of two unequal distributed Bragg reflecting mirrors (DBR) [7,41]. In order to apply electric fields on the QDs, the top (bottom) DBR was n- (p-) type doped. For charging the QD in a controllable way, a 10nm thick AlAs barrier was placed inside the cavity, between the QDs and the top, p-type doped mirror [28]. This barrier prolongs the tunneling time of heavy-holes into the QDs at forward bias and out of the QDs at reverse bias, while marginally affecting the tunneling time of electrons. As a result, negative charging is facilitated upon forward bias and positive charging upon reverse bias.

Figs. 7a-d show the measured PL and linear polarization spectra of a single QD from this sample, under two external bias voltages. At zero bias (Fig. 7a, b) the charge state is between -1 and +1, while at forward bias (Fig. 7c, d) it is between -3 and -1. The various lines are marked by their initial state and where needed, their final state is also indicated. Figs. 7e-h show the corresponding calculated spectra.

In Fig. 8, the measured polarized fine structure of various lines is compared with the calculated one. While most of the measured intensity ratios, relative PL energies and polarization degrees and directions are reproduced by the theory discussed above, some measured spectral lines show unexpected polarization directionality. We find spectral lines with linear polarization axes

rotated clockwise by  $67.5^\circ$  relative to the H and V axes. These rotated polarization directions,  $V+\bar{D}$  and  $H+D$ , respectively, which roughly coincide with the  $[1, 2, 0]$  and  $[2, -1, 0]$  crystalline directions, appear only in spectral lines associated with configurations containing one unpaired  $p_x$ -shell charge carrier:  $X^{-2}$ ,  $XX^{-1}$ , and  $XX^{+1}$ . Other configurations, which contain only s-shell charge carriers or either closed shells or two unpaired p-shell carriers ( $p_x$  and  $p_y$ ), the linear polarizations are along the H and V axes. The simple single band, single carrier, model that we presented above, is insensitive to the crystalline directions and cannot explain these observations.

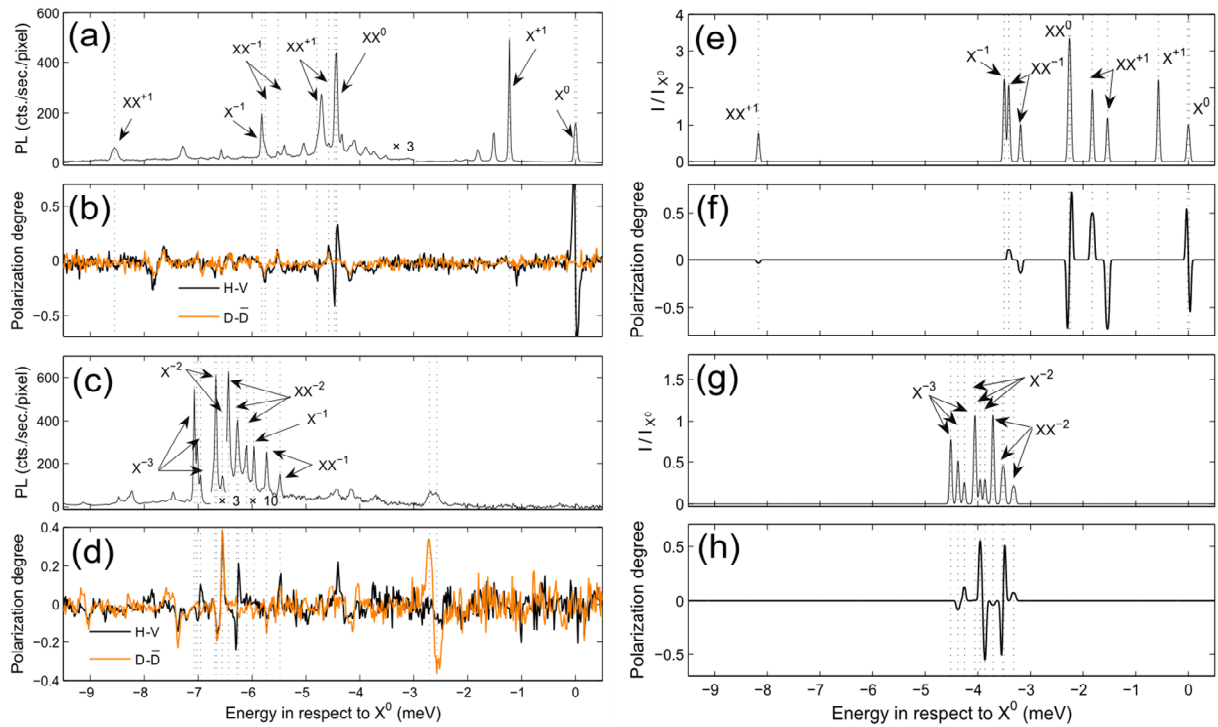


Fig. 7. [(a) and (c)] Measured PL spectra for bias voltages of 0 and 7.15 V, respectively. The energy is measured from the energy of the  $X^0$  line. [(b) and (d)] PL linear polarization spectra for bias voltages of 0 and 7.15 V, respectively. The black (orange) line presents projection on the H-V ( $D-\bar{D}$ ) direction. [(e) and (g)] and [(f) and (h)] Calculated PL and PL linear polarization (projected on the H-V direction) spectra for various single QD excitonic transitions. Vertical dotted lines at various spectral lines are drawn to guide the eye.

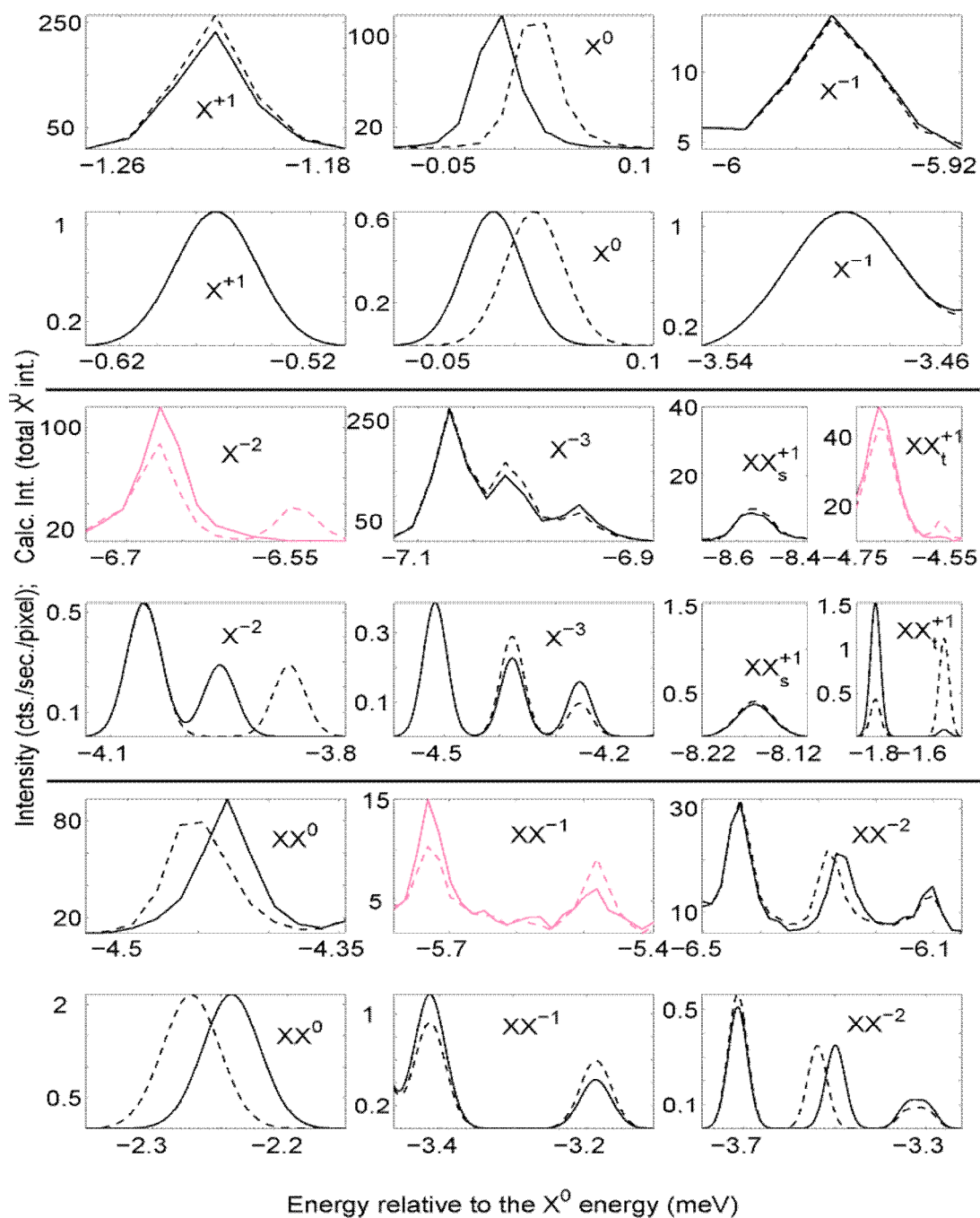


Fig. 8. Measured (top panel in each pair) and calculated (bottom panel in each pair) high resolution polarization sensitive PL spectra for various spectral lines. The solid (dashed) black line represents H (V) polarized spectrum, while the solid (dashed) gray line represents V+D (H+D) polarized spectrum.

### *Carrier dynamics in quantum dots*

In this section we discuss two experimental methods for probing the dynamics of confined charge carriers in QD: Polarization memory measurements and polarization sensitive intensity correlation measurements. The theory that we use in order to gain intuition and to understand the dynamics of photoexcited carriers in these nanostructures from the analysis of these experimental results is thoroughly discussed.

#### *Polarization memory in quasi resonant excitation*

In a polarization memory measurement, the system is excited by a polarized light, and the polarization of the PL emission is measured. If the polarization of a certain spectral line is the same as (opposite to) that of the exciting light, the line is said to have positive (negative) polarization memory. In general, the degree of polarization memory depends on the specific spectral line, its polarization and the energy to which the exciting light is tuned. The degree of circular polarization memory (DCPM) and the degree of linear polarization memory (DLPM) along the major axes of the QD are defined as

$$P_{circ} = \frac{I_+^+ - I_-^+}{I_+^+ + I_-^+} \quad P_{lin} = \frac{I_H^H - I_V^H}{I_H^H + I_V^H} \quad (1.25)$$

where  $I$  stands for the PL intensity, and the superscript (subscript)  $+$  ( $-$ ) or  $H$  ( $V$ ) stands for right- (left-) hand circular polarization, or horizontal- (vertical-) linear polarization of the exciting (emitted) light. The horizontal (vertical) direction is determined by the polarization direction of the lower (higher) energy fine-structure component of the neutral exciton ( $X^0$ ) line, (see Fig. 5a). Usually, when a QD is excited well above the band-gap of the host material (non-resonant excitation), no polarization memory is observed. This is due to fast spin scattering of both types of charge carriers during their relaxation from the continuum to the QD states [42, 43]. When the

excitation energy is below the continuum of the QD or its wetting layer bandgap, we refer to it as to a quasi resonant excitation. In this case the situation is different, and some polarization memory is observed. Resonant excitation into well defined low energy optical resonances of the QDs, will not be reviewed here.

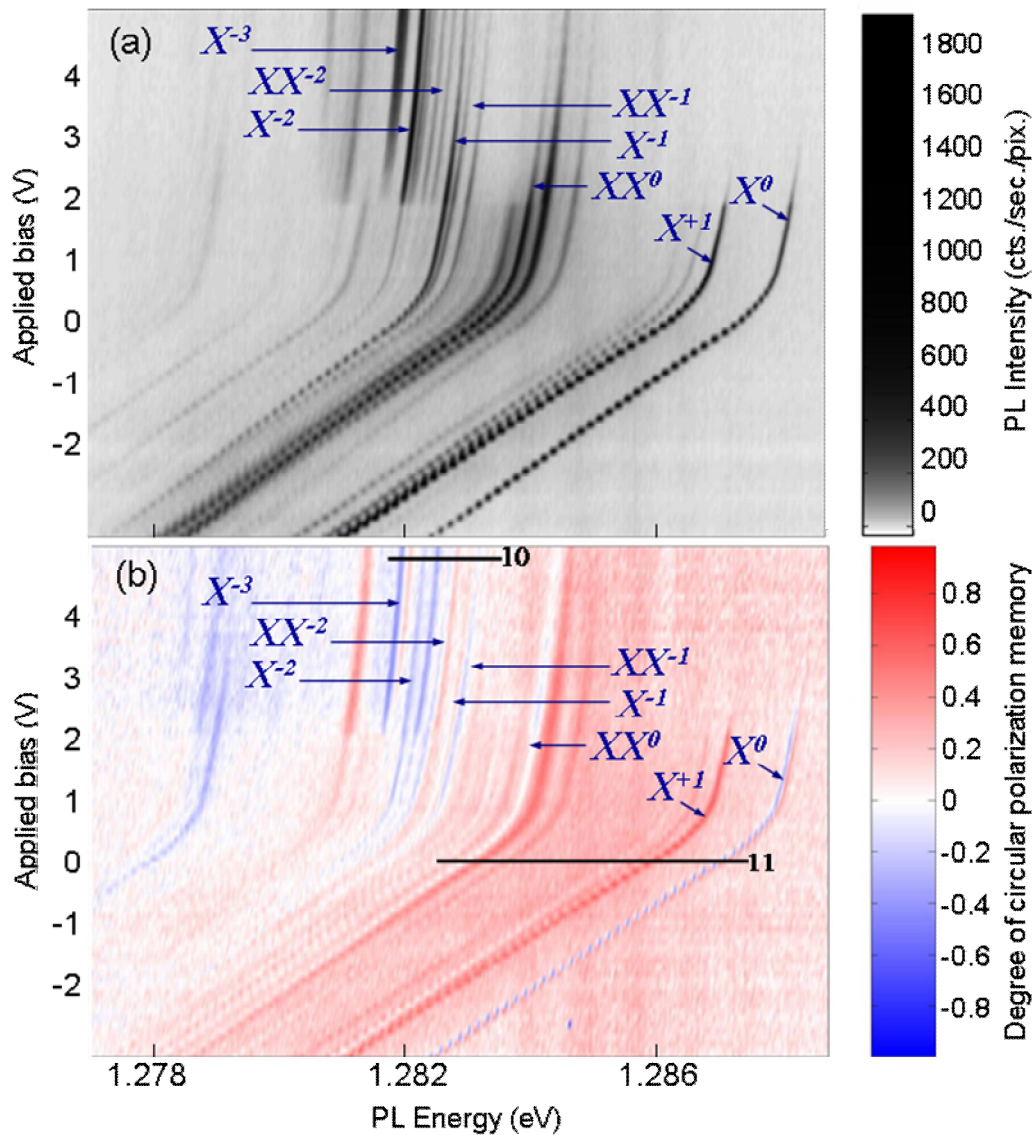


Fig. 9. Bias dependent PL spectra (a) and DCPM (b) from a single QD excited at 1.369 eV. The black horizontal lines marked 10 and 11 indicate the bias and spectral ranges from which Figs. 10 and 11 were obtained.

For quasi resonant excitations, we find that different lines show different DCPM. However, none of the observed lines show any DLPM. The data and its discussion are presented below.

In Fig. 9a we present bias dependent photoluminescence (PL) spectra from the same QD discussed above, optically excited at 1.369 eV. At this energy, a few meV below the bandgap of the InAs wetting layer, the QDs are quasi-resonantly excited [44]. At reverse bias the spectral lines are red-shifted due to the applied electric field, and lines due to optical transitions in the presence of positive charges are enhanced. At forward bias, flat-band conditions are reached and spectral lines due to the presence of negative charges appear, while lines in the presence of positive charges disappear. The various spectral lines are identified by their bias dependence and their order of appearance as the bias increases. As described above, their identifications also rely on their polarized fine structure [28].

In Fig. 9b we present the DCPM spectra as a function of the bias applied on the QD. Clearly, the DCPM of each and every spectral line is almost bias independent. In general, it is obvious that while all positive lines have positive DCPM, various negative lines have negative DCPM signs.

In Fig. 10a we present spectra of various spectral lines as obtained at a forward bias of 4.9 V. At this voltage the QD is negatively charged with either, one, two, or three electrons. The solid (dashed) line represents the spectrum obtained when the excitation and collection are co-(cross-) circularly polarized. In Fig. 10b we present the corresponding DCPM. In Fig. 10 one clearly sees that the DCPM sign depends on the specific optical transition. Some spectral lines show positive memory, like all the lines associated with positive charges do. Some show no polarization memory, and some show negative polarization memory. In Fig. 11a we present the spectrum obtained at 0 V. In Fig. 11b we present the measured DCPM and DLPM. The  $X^0$  line shows no DCPM, and in total no DLPM either, since its H and V polarized fine-structure components are

equally visible upon H linearly polarized excitation. We note that the  $X^{+1}$  (positively charged exciton) shows strong positive DCPM but no DLPM.

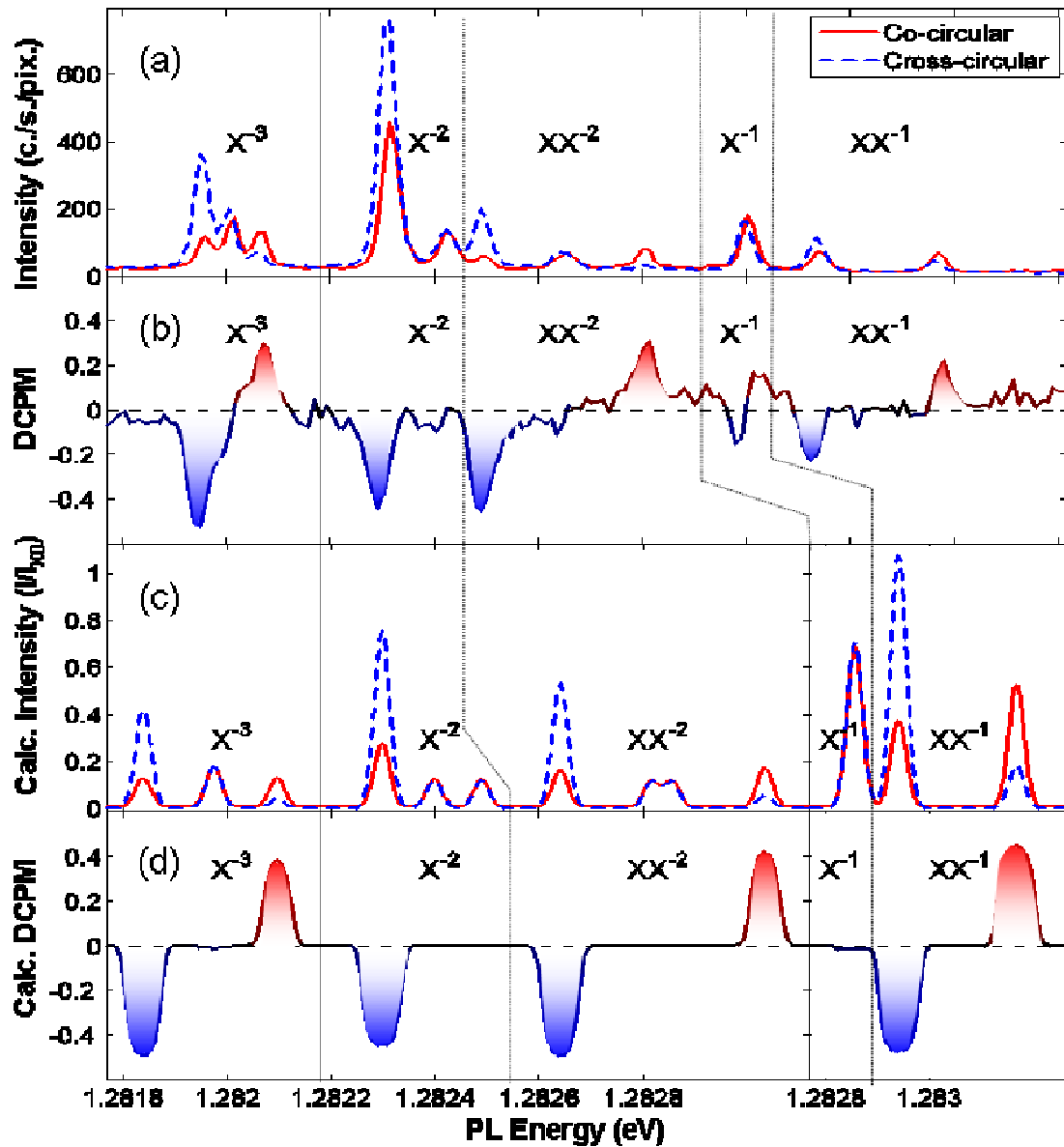


Fig. 10. (a) Measured and (c) calculated polarization sensitive spectra at 4.9 V. The solid (dashed) line represents spectrum obtained with co- (cross-)circularly polarized excitation and detection:  $I_{\text{co}} = I_{+}^{+}$  ( $I_{\text{cross}} = I_{-}^{+}$ ). (b) Measured and (d) calculated degree of circular polarization memory. The dotted vertical lines are guides to the eye.

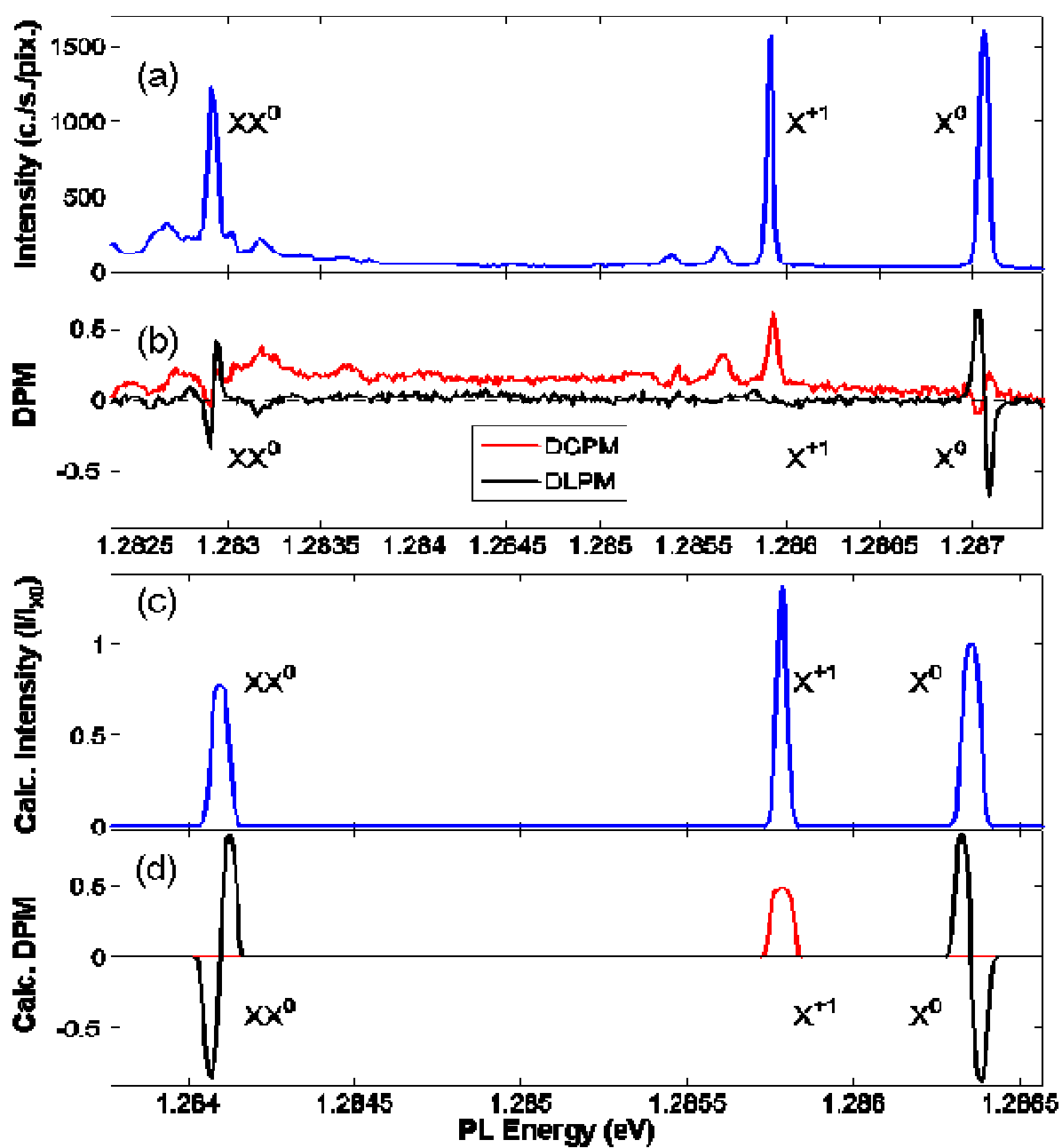


Fig. 11. (a) Measured and (c) calculated polarized PL spectra at 0 V. (b) Measured and (d) calculated degrees of circular (gray line) and linear (black line) polarization memory.

### *Spin scattering rates*

In order to explain these observations and to gain further insight into the phenomenon of polarization memory in quasi-resonantly optically excited single semiconductor quantum dots, we use the single band, full configuration-interaction model described in the previous sections. We use the model to calculate the quantum dot's confined many-carrier states and the selection rules for optical transitions between these states. Prior to the excitation, the states within 1 meV from the ground state of a given number of  $N_h$  holes and  $N_e$  electrons are considered to be populated with equal probability. This assumption is compatible with thermal distribution at the ambient temperature in which the experiment was held ( $\sim 20\text{K}$ ). We consider the polarized quasi-resonant excitation at a given polarization by adding an additional electron-hole pair to these states. The spin state of the additional carriers are defined by their initial spin polarization,  $S_{exc}$ , dictated by the polarization of the exciting light, and by their spin dephasing rate during thermalization. Quite generally, we describe the spin orientation loss by four probabilities which apply to each carrier independently. The probabilities  $p_j^{e,h}$  are for either spin orientation preservation,  $j=0$ , or for spin rotations by  $\pi$  radians about the spatial directions x, y, and z for  $j=1, 2$  and  $3$ , respectively. The spin states of the thermalized pair can now be represented by a 4-by-4 density matrix in the Hilbert space of the pair's spin states:  $\{\downarrow\uparrow, \uparrow\downarrow, \uparrow\uparrow, \downarrow\downarrow\}$ :

$$\rho^{th} = \sum_{j,j'=0}^3 p_j^e p_{j'}^h \sigma_j^e \otimes \sigma_{j'}^h |S_{exc}\rangle \langle S_{exc}| \sigma_j^{e\dagger} \otimes \sigma_{j'}^{h\dagger} \quad (1.26)$$

where  $\sigma_j^{e(h)}$  are the Pauli matrices acting on the sub-space of electron ( $\uparrow$ ) (hole ( $\uparrow$ )) spin states, and  $\sigma_0$  is the unit matrix. The operation  $\otimes$  is the Kronecker product. In Eq. (1.26) we used the identity:  $\exp(i\pi \cdot \frac{1}{2} \sigma_j) = i\sigma_j$ . If one further assumes that the spin orientation loss (or dephasing)

for both carrier types is isotropic, then the number of independent probabilities to be considered is reduced to two,  $p^e$  and  $p^h$ , where,

$$p_1^{e(h)} = p_2^{e(h)} = p_3^{e(h)} \equiv p^{e(h)} ; \quad p_0^{e(h)} = 1 - 3p^{e(h)} \quad (1.27)$$

We note here that the probabilities  $p^e$  and  $p^h$  can be written in terms of the spin-dephasing time  $T_2^*$  [45] and the thermal relaxation time  $\tau$ , as:

$$p^{e(h)} = \tau^{e(h)} / (4\tau^{e(h)} + T_2^{*e(h)}) \quad (1.28)$$

These relations arise from the master equations (see below) describing a single charge carrier undergoing simultaneous spin-dephasing and thermal relaxation from its orbital state.

The photogenerated pair increases the number of charge carriers to  $N_h+1$  holes and  $N_e+1$  electrons. The new many-carrier states are restricted to these many-carrier states which accommodate the photogenerated carriers with their spin orientation. For an initial state  $|A\rangle$  of  $N_e$  electrons and  $N_h$  holes, the resulting density matrix which defines the states with the additional thermalized pair is given by

$$\rho_A = \sum_{\alpha, \beta} \rho_{\alpha\beta}^{th} \hat{x}_\alpha^\dagger |A\rangle \langle A| \hat{x}_\beta \quad (1.29)$$

where  $\hat{x}_\alpha^\dagger$  is the creation operator of an electron-hole pair with spin  $\alpha$  in any combination of single electron and single hole spatial states:

$$\hat{x}_\alpha^\dagger = \sum_{m,n} \hat{a}_{m,\alpha_e}^\dagger \hat{b}_{n,\alpha_h}^\dagger \quad (1.30)$$

Here  $\hat{a}_{m,\alpha_e}^\dagger$  ( $\hat{b}_{n,\alpha_h}^\dagger$ ) is the creation operator of an electron (a hole) in the single electron (hole) spatial state  $m$  ( $n$ ), with spin state  $\alpha_e$  ( $\alpha_h$ ). With this notation the spin state of the electron-hole pair is given by  $\alpha \equiv \{\alpha_e, \alpha_h\}$ . With this description of the  $N_e+1, N_h+1$  many carrier state, we

proceed by projecting it on all the possible ‘ground’ states  $|G\rangle$  within 1 meV of the lowest energy level of  $N_e+1, N_h+1$  charge carriers. Recombination of one e-h pair from these states, actually gives rise to the PL signal.

We conclude by calculating the energies  $\varepsilon$  and the relative intensities of polarized optical transitions  $I_{S_{em}}^G(\varepsilon)$  with polarization  $S_{em}$  from the ground states  $|G\rangle$  to the many body states of  $N_h$  holes and  $N_e$  electrons [29, 46]. The  $S_{em}$  polarized spectrum resulting from  $S_{exc}$  polarized quasi-resonant excitation is finally obtained by summing over all the thermally populated initial states  $|A\rangle$  and over all optically excited  $|G\rangle$  states contributing to the photoluminescence:

$$I_{S_{em}}^{S_{exc}}(\varepsilon) = \sum_{G,A} Tr(\rho_A |G\rangle\langle G|) \cdot I_{S_{em}}^G(\varepsilon) \quad (1.31)$$

We note that  $\rho_A$  is obtained from the polarization of the exciting light  $|S_{exc}\rangle$  via Eqs. (1.26) through (1.30). The two probabilities in Eq. (1.27)  $p^e$  and  $p^h$  can now be extracted from the measured DCPM and DLPM by fitting them to the calculated ones. The values  $p^e = 1/8$  and  $p^h = 1/4$  describe very well the observations for this particular quasi-resonant excitation. In accord with Eq. these values mean that while the hole’s dephasing time is much shorter than its relaxation time, and thus it totally loses its spin polarization during the thermalization, the electron’s degree of polarization is reduced only by one half, meaning that its dephasing and relaxation times are comparable. Kalevich et al. [47] used previously a similar assumption to successfully explain their observation of negative circular polarization memory in an ensemble of doubly-negatively charged QDs.

The calculated spectra for co- and cross-circularly polarized emission from a negatively charged quantum dot with 1 up to 3 charges were added together to form the calculated polarization

sensitive spectra in Fig. 10c. Both single exciton and biexciton emissions were included.

Gaussian broadening of 35  $\mu\text{eV}$  was assigned for each optically allowed transition. The calculated DCPM spectrum is presented in Fig. 10d. By comparing the measured and calculated polarization sensitive spectra and DCPM, one clearly notes that all the features of the measured DCPM are given by this simple model.

In Fig. 11c we present the calculated spectrum for the neutral exciton ( $X^0$ ), the neutral biexciton ( $XX^0$ ), and the singly positively charged exciton ( $X^{+1}$ ). In Fig. 11d we present the corresponding calculated DCPM (gray) and DLPM (black). The H (V) directions are along the long (short) semi-axes of the model QD [28]. The positive DCPM of the  $X^{+1}$  spectral line and the lack of DCPM from the neutral excitonic transitions are clearly reproduced by our model. In addition, the model clearly reproduces the experimentally measured lack of DLPM from all the observed spectral lines at this quasi-resonant excitation energy. We note here, however, that DLPM is observed in some cases of resonant excitations [48-51]. In these cases, (to be presented elsewhere), both the electron and the hole retain at least part of their initial spin polarization during their thermalization, before they recombine.

Intuitively, one can easily comprehend the observed DCPM phenomena as a consequence of the isotropic-EHEI induced energetic separation between states where the electron and hole spins are parallel to those where they are anti-parallel. Since circularly polarized excitation and emission always involve electron-hole pairs with anti-parallel spins, states with (anti-) parallel spins can be reached only in cases where one (none) of the carriers flips its spin. This simple reasoning leads to negative (positive) circular polarization memory. As an illustration for the processes which lead to polarization memory, we schematically describe in Fig. 12 the case of quasi-resonant excitation of the  $X^{-3}$  spectral line.

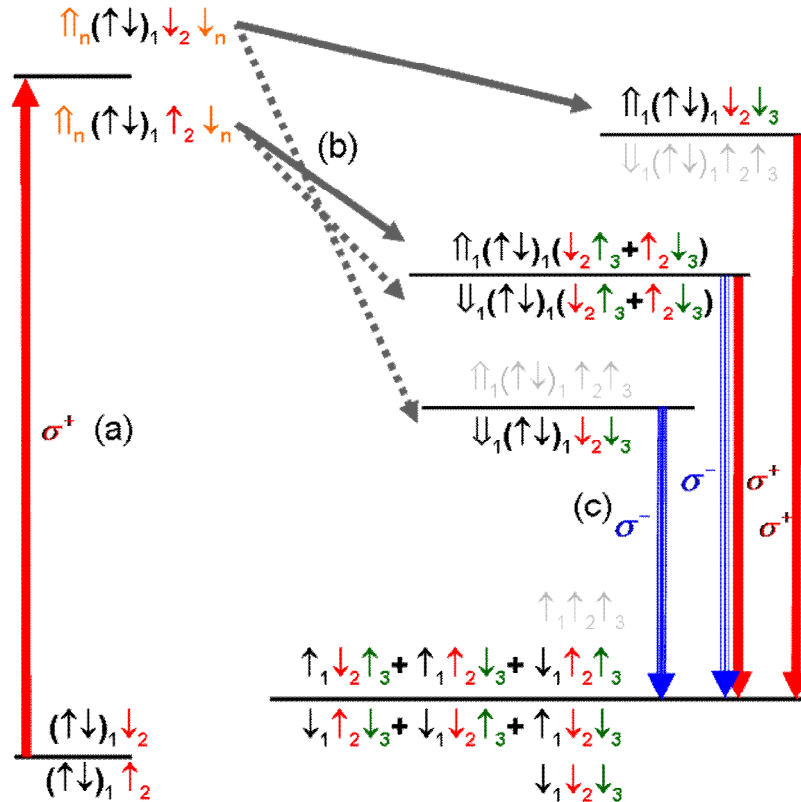


Fig. 12. Schematic description of the processes which lead to the observed DCPM among the  $X^3$  spectral lines. The symbol  $\uparrow(\downarrow)$  represents a spin up (down) hole (electron). The subscript near each symbol denotes the particle's energy level (see Fig. 3). Gray color represents states which do not participate in the described process. (a) An electron-hole pair is photogenerated in high lying energy levels (denoted by the subscript 'n') by a quasi-resonant  $\sigma^+$  polarized excitation and added to three QD electrons residing in their ground states. (b) During the thermalization, the hole spin projection along the growth direction is either preserved (solid dark-gray arrows), or flipped (dotted dark-gray arrows). The lowest (highest) energy level of the ground  $N_e=4$ ,  $N_h=1$  states, is reached only if the hole flips (preserves) its spin orientation. The intermediate level is reached in both cases. (c) All three levels return via radiative recombination of an s shell electron hole pair to the same four-fold degenerate  $N_e=3$ ,  $N_h=0$  level, giving rise to spectral lines with positive, negative and no DCPM, respectively.

Before we conclude this discussion we note that the appearance of negative DCPM in the lowest energy doublet of the doubly negatively charged exciton ( $X^{-2}$ ), indicates that the energy splitting between the two components of this doublet is smaller than the radiative width of the lines [47, 51]. Consequently, we set this particular anisotropic EHEI energy to zero in our model [28].

### *Polarized intensity correlation spectroscopy*

The intensity (second order) correlation function between two spectral lines, A and B is defined as:

$$g_{A,B}^{(2)}(\tau) = \frac{\langle I_A(t) I_B(t+\tau) \rangle_t}{\langle I_A(t) \rangle_t \langle I_B(t) \rangle_t} \quad (1.32)$$

where  $I_{A(B)}$  is the intensity of line A (B), and  $\langle \rangle_t$  means averaging over the time  $t$ . If B=A the function is known as the intensity autocorrelation function, and is commonly used to demonstrate quantum light or single photon sources [4-6].

Emission of a photon from line A at time  $t$  sets the system to the final state of the relevant optical transition. Therefore,  $\langle I_A(t) I_B(t+\tau) \rangle_t = \langle I_A(t) \rangle_t \langle I_{B/A}(t+\tau) \rangle_t$ , where  $I_{B/A}(t+\tau)$  is the intensity of transition B at time  $t+\tau$  *conditional* on the system being in the final state of transition A at time  $t$ . Furthermore, the intensity of an optical transition is proportional to the population probability of its initial state (Eq. (1.23)). Therefore, for  $\tau > 0$ ,

$$g_{A,B}^{(2)}(\tau > 0) = \frac{\langle I_A(t) \rangle_t \langle I_{B/A}(t+\tau) \rangle_t}{\langle I_A(t) \rangle_t \langle I_B(t) \rangle_t} = \frac{\langle I_{B/A}(t+\tau) \rangle_t}{\langle I_B(t) \rangle_t} = \frac{P_{B/A}(\tau)}{P_B^{SS}} \quad (1.33)$$

where  $P_{B/A}(\tau)$  is the average population at time  $\tau$  of the initial state of transition B with the condition that the state of the system at time 0 was the final state of transition A. The steady-state

probability to find the system in the initial state of transition B,  $P_{B/A}(\tau \rightarrow \infty)$ , is denoted by  $P_B^{SS}$ .

At negative time differences ( $\tau < 0$ ), the role of the two transitions is simply exchanged.

$$g_{A,B}^{(2)}(\tau < 0) = g_{B,A}^{(2)}(|\tau|) = \frac{P_{A/B}(|\tau|)}{P_A^{SS}} \quad (1.34)$$

This simple analysis shows the usefulness of intensity correlation measurements as a tool for studying QD carriers' population dynamics.

Experimentally, intensity correlation measurements are usually performed using a Hanbury Brown and Twiss apparatus (HBTA) [52]. The apparatus that we constructed provides the necessary means to temporally correlate between the emission intensities of two spectral lines, each one of them projected onto any desired polarization state. The apparatus is schematically described in Fig. 13.

The emitted light from the sample is split into two beams by a non polarizing beam splitter. By two monochromators, and two sets of polarizers and variable retarders, we select the desired spectral line at the desired polarization in each arm of the apparatus. A silicon avalanche photodetector in each arm detects a single photon and converts it to a current pulse. The time difference between the pulses from the two detectors is repeatedly measured using a time to analog converter. A multi channel analyzer then builds a histogram of time differences between the detection times of the two photons. In continuous wave (cw) measurements the histogram can be straight forwardly normalized by its value at long time differences, to yield the intensity correlation function.

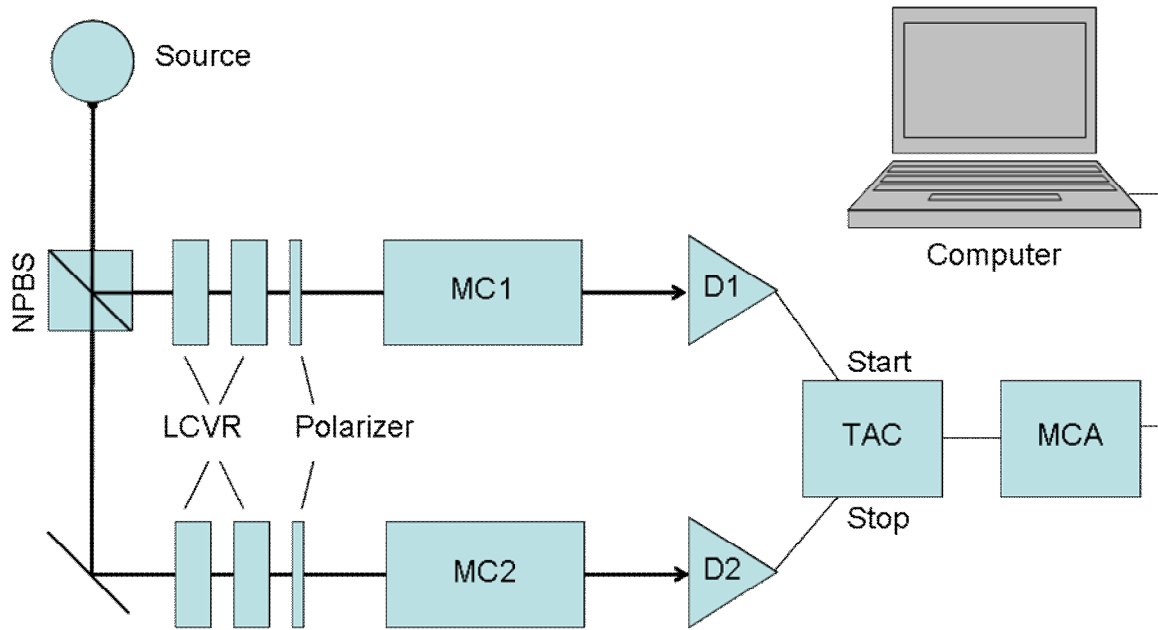


Fig. 13. Schematic illustration of a Hanbury-Brown and Twiss apparatus. NPBS – Non polarizing beam splitter. LCVR – Liquid crystal variable retarder. MC – Monochromator. D – Detector. TAC – Time to analog converter. MCA – Multi-channel analyzer.

### *Rate equations and Master equations*

In order to calculate the correlation functions, we calculate first the population probabilities. For energetically distinct levels, coherence effects can be neglected, and the populations can be calculated using a set of coupled classical rate equations [53]. Where by ‘energetically distinct’ we mean that the energetic distance between the levels is much wider than their total width. The set of classical rate equations can be generally written in the following form [40, 53],

$$\dot{\vec{n}}(t) = \vec{R}(t)\vec{n}(t) \quad (1.35)$$

Here  $\vec{n}(t)$  is a vector of level populations and  $\vec{R}(t)$  is a matrix containing the transition rates between all the levels involved. In cw excitation, the detected first photon sets the starting conditions, and then, Eq. (1.35) can be solved quite straightforwardly if the matrix  $\vec{R}(t)$  is

known [53].

When coherence matters, classical rate equations are not sufficient. A more general approach is formulated by a set of coupled Master equations acting on the density matrix instead of on the populations only. Lindblad formulated the problem in the most general form [54],

$$\dot{\rho}(t) = -\frac{i}{\hbar}[H, \rho(t)] + \sum_k \left( L_k \rho(t) L_k^\dagger - \frac{1}{2} \rho(t) L_k^\dagger L_k - \frac{1}{2} L_k^\dagger L_k \rho(t) \right) \quad (1.36)$$

Here  $\rho$  is the density matrix,  $H$  is the Hamiltonian, and  $\{L_k\}$  describe non unitary processes.

For example, a transition between the state  $i$  and the state  $f$  with a rate  $\Gamma_{fi}$  is described by

$$L_{fi} = \sqrt{\Gamma_{fi}} |f\rangle\langle i|; \text{ Pure dephasing of the state } i \text{ with a rate } \Gamma_i^d \text{ is described by } L_i^d = \sqrt{\Gamma_i^d} |i\rangle\langle i|.$$

Similarly to Eq. (1.35), Eq. (1.36) can be written in a vector form,

$$\dot{\vec{\rho}}(t) = \vec{\mathcal{L}}(t) \vec{\rho}(t) \quad (1.37)$$

Here  $\vec{\rho}(t)$  is a column vector formed from the columns of the density matrix, and  $\vec{\mathcal{L}}(t)$  is the following matrix:

$$\vec{\mathcal{L}}(t) = -\frac{i}{\hbar} \left( I \otimes H - H^T \otimes I \right) + \sum_k \left( \left( L_k^\dagger \right)^T \otimes L_k - \frac{1}{2} \left( L_k^\dagger L_k \right)^T \otimes I - \frac{1}{2} I \otimes L_k^\dagger L_k \right) \quad (1.38)$$

Here  $I$  is the unit matrix,  $\otimes$  means Kronecker product, and  $^T$  means transposition. As is the case of the classical rate equations, Eq. (1.37) can be solved quite straightforwardly.

Once the populations and the coherences are found, Eq. (1.33) is used to find the intensity correlation function. Specifically, the intensity correlation function between a photon leading to the state  $\rho_1$  (or  $\vec{n}_1$ ), and the photon emitted from the state  $\rho_2$  (or  $\vec{n}_2$ ) is given by

$$g_{\rho_1, \rho_2}^{(2)}(\tau) = \frac{\text{Tr} \left( \rho_2 \cdot \rho(\tau) \Big|_{\rho(0)=\rho_1} \right)}{\text{Tr}(\rho_2 \cdot \rho_{SS})} \quad \text{or,} \quad g_{\vec{n}_1, \vec{n}_2}^{(2)}(\tau) = \frac{\vec{n}_2 \cdot \vec{n}(\tau) \Big|_{\vec{n}(0)=\vec{n}_1}}{\vec{n}_2 \cdot \vec{n}_{SS}} \quad (1.39)$$

where  $\rho_{SS}(\vec{n}_{SS})$  is the density matrix (populations) at long time differences ( $\tau \rightarrow \infty$ ) – the steady state solution.

### ***Radiative cascades***

By radiative cascade we mean correlated emission of two or more photons. Radiative cascade usually occurs when a second photon is emitted within its radiative lifetime after the emission of a first photon. We distinguish here between two types of radiative cascades: direct ones and indirect ones. In a direct radiative cascade, the state of the system after the emission of the first photon is the state from which the second photon is emitted (Fig. 14a). In an indirect cascade, a mediating process occurs between the two emissions, and the second photon is not emitted from the final state of the first emission (Fig. 14b). Clearly, the mediating process rate should be faster or comparable to the radiative rate in order for the two emissions to form a radiative cascade. Experimentally, a radiative cascade reveals itself in the measured intensity correlation function between two or more relevant spectral lines. It always gives rise to “bunching” at  $\tau \geq 0$  and “antibunching” at  $\tau \leq 0$ . Here by “bunching” (“antibunching”) we mean that the intensity correlation function obtains values which are greater (smaller) than 1. These reflect the fact that there is a definite order between the two emissions and that right after the emission of the first photon, the probability for the emission of the second photon is greater than its average value. In other words emission of the second photon cannot precede the emission of the first one and that ordered emission of photon pairs is preferred over uncorrelated emissions.

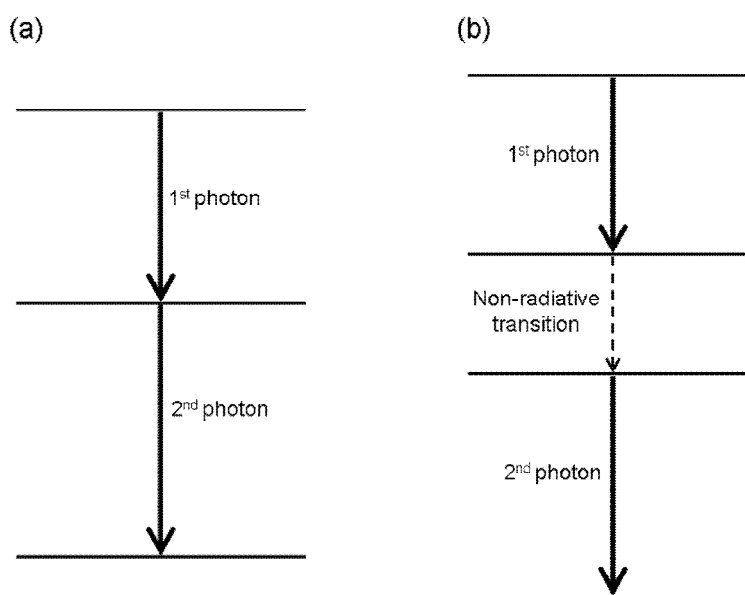


Fig. 14. Schematic description of two types of radiative cascades: (a) A direct cascade. (b) An indirect cascade.

In the following we discuss several examples of direct and indirect radiative cascades in single semiconductor quantum dots.

#### *The neutral biexciton cascade*

The most studied [7, 8, 53, 55-57] radiative cascade in semiconductor QDs is the neutral biexciton cascade. The initial state is a ground-state biexciton: two electrons and two holes occupying their respective lowest energy levels. Due to Pauli's exclusion principle, both carrier pairs form spin-singlets with total spin 0. Optical recombination of one e-h pair results in the emission of a single photon, and a single e-h pair (bright exciton) remains in the QD. This pair then recombines within its radiative lifetime, resulting in emission of a second photon. At the end of the cascade the QD is left empty of carriers. This cascade is a direct one, as the single bright exciton is both the state at which the first photon emission ends and the state from which

the second photon emission occurs. As described in Fig. 15, this intermediate level has two spin states. Therefore, since the transition rate from one spin state to the other is very slow (relative to the radiative lifetime) the cascade has two distinctive paths along which it can proceed.

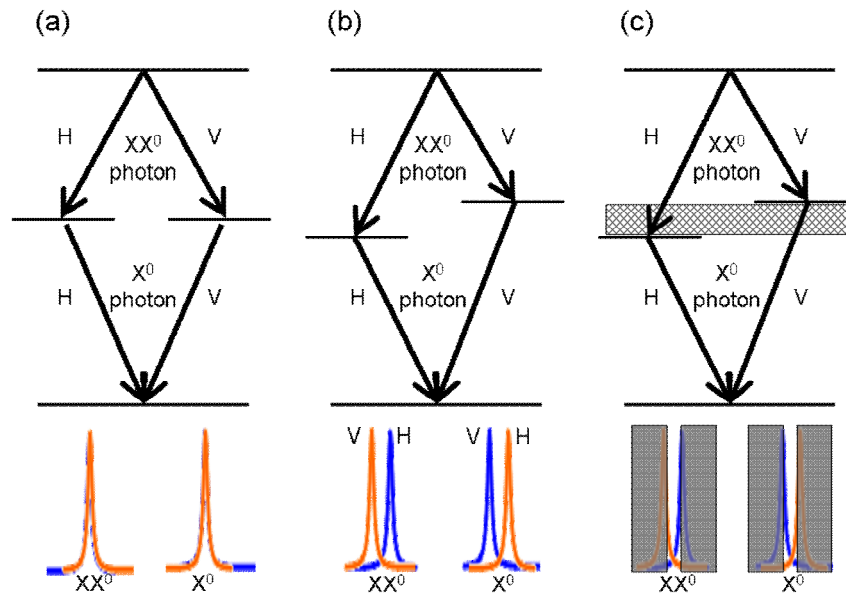


Fig. 15. Schematic descriptions of the neutral biexciton radiative cascades (top) and PL spectra (bottom). (a) Degenerate exciton levels. (b) Split exciton levels. (c) Split exciton levels and spectral filters for entanglement distillation.

Due to the different selection rules for the two bright exciton spin-states, the two paths differ by the polarization of the emitted photons. If the intermediate state is degenerate, then this is the only difference (Fig. 15a) and the two photons are polarization-entangled [55]. However, as discussed above, any anisotropy in the QD shape, strain distribution etc., lifts the degeneracy between the two bright exciton levels through the anisotropic EHEI (Fig 15b). When the levels are split, the two paths are also distinct by their photons' energies. This distinction reveals the information about "which path" the cascade occurs. Therefore, the degree of entanglement in the two photons polarization state becomes very low, and their polarization state is said to be

classically correlated only: In each path the two photons are co-linearly polarized. The degree of entanglement depends on the ratio between the radiative width of the spectral lines and the splitting energy. There have been attempts to reduce the splitting energy by use of several techniques. Those include application of external fields (static [58] and alternating [59] electric fields, magnetic fields [60], strain [61]), or modification of the growth process (thermal annealing [62], growth along a different crystallographic direction [63]). Some of these techniques were successful, and recently there have been several demonstrations of the emission of entangled photon pairs from QDs using such techniques [8, 59, 63]. Alternatively, even if the splitting energy is larger than the radiative lifetime, entangled photons can still be produced by spectral filtering [7] (Fig. 15c). Spectral filters post-select only photons emitted in the energy regions between the two fine-structure components of both the biexciton and exciton emissions. In these regions, the energies of the photons in both paths are similar such that they do not reveal the “which path” information, and the entanglement is partially restored. Indeed, the very first demonstration of entangled photons from radiative cascades in QDs [55] was achieved this way [7].

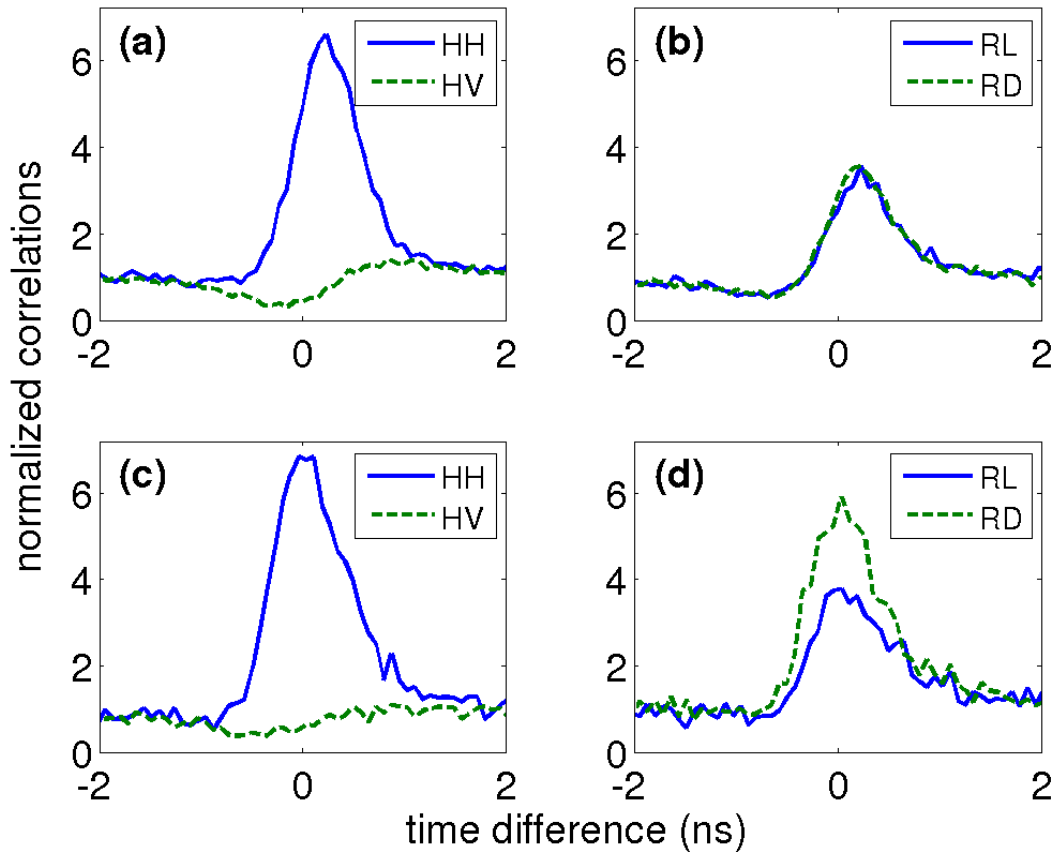


Fig. 16. Measured polarization sensitive intensity correlation functions between the  $XX^0$  and the  $X^0$  lines for various polarization combinations. (a) and (b), no spectral filtering. (c) and (d), with spectral filtering. The first (second) letter in each legend item specifies the polarization of the  $XX^0$  ( $X^0$ ) photon: H – horizontal, V – vertical, D – diagonal, R – right-hand circular, L – left-hand circular. The coincidence rate at long time differences for (a) and (b) [(c) and (d)] is 5 [0.5] per minute per time bin (80ps).

Figs. 16a and 16b show polarization sensitive measured correlation functions between the biexciton ( $XX^0$ ) and the exciton ( $X^0$ ) lines, without any spectral filtering (photons from both fine-structure components arrive at the detectors), for co- and cross-linear polarizations (a) and

for circular-circular and circular-diagonal polarization combinations (b). It is seen that for co-linear polarizations the exciton photons “bunch” immediately after the biexciton is detected. The probability of two photons to be emitted together (at zero time delay) is *at least 7* times larger than their average emission probability. The actual bunching is probably larger as the correlation function is smeared by the finite temporal resolution ( $\sim 300$  ps) of the detectors.

For cross-linear polarizations the opposite happens: at small time differences the emission probability of a cross-linearly polarized photon-pair almost vanishes. This “antibunching” proves experimentally that the rate of cross-transitions between the exciton states is negligible relative to the radiative rate. The pairs of photons are always emitted with the same linear polarization. Different other polarization sensitive correlation measurements are all similar. For example, there is no difference between circular-circular and circular-diagonal polarization combinations. All show the same bunching signal, which amounts to one half of the signal in co-linear polarizations. This shows that preferred correlations exist only in the rectilinear basis, and thus the photons are only classically correlated, but not entangled [57].

The situation is different when spectral filtering is applied. In Figs. 16c and 16d we present measured correlation functions with spectral filtering. A pronounced difference is observed between correlations in circular-circular and circular-diagonal polarization combinations.

In order to unambiguously prove entanglement in radiative cascades, however, one should construct a set of measurements and demonstrate violation of the Bell inequality [64-67].

Another way is to construct by polarization tomography the entire density matrix of the two photon state [68]. This is done by measuring the  $XX^0-X^0$  correlation function in 16 different polarization combinations. For each measurement, the number of events coming from the same cascade is extracted by integrating the background-reduced correlation function. The background

in these measurements is readily available from the measurements in cross-linear polarizations [7]. In this case all the measured events do not result from the same radiative cascade. Rather they result from cases in which the detected two photons were emitted in two different cascades. Therefore, they truly represent the background due to the cw nature of the experiment. Since this background is insensitive to the polarizations of the two photons, it can be safely subtracted from all the measured, normalized, intensity correlation functions.

The density matrix fully described the system, and there are a few tests which can be applied to it in order to quantify the degree of entanglement between the polarization states of the emitted pair of photons. We use the Peres criterion, which states that a density matrix is entangled if its partial transpose has negative eigenvalues [69].

Fig. 17 shows the measured density matrices without (a) and with (b) spectral filtering. While the matrix in Fig 17a fails to satisfy the Peres criterion within the measurement uncertainty, the matrix in Fig 17b satisfies it with a confidence level which is better than 3 standard deviations [7].

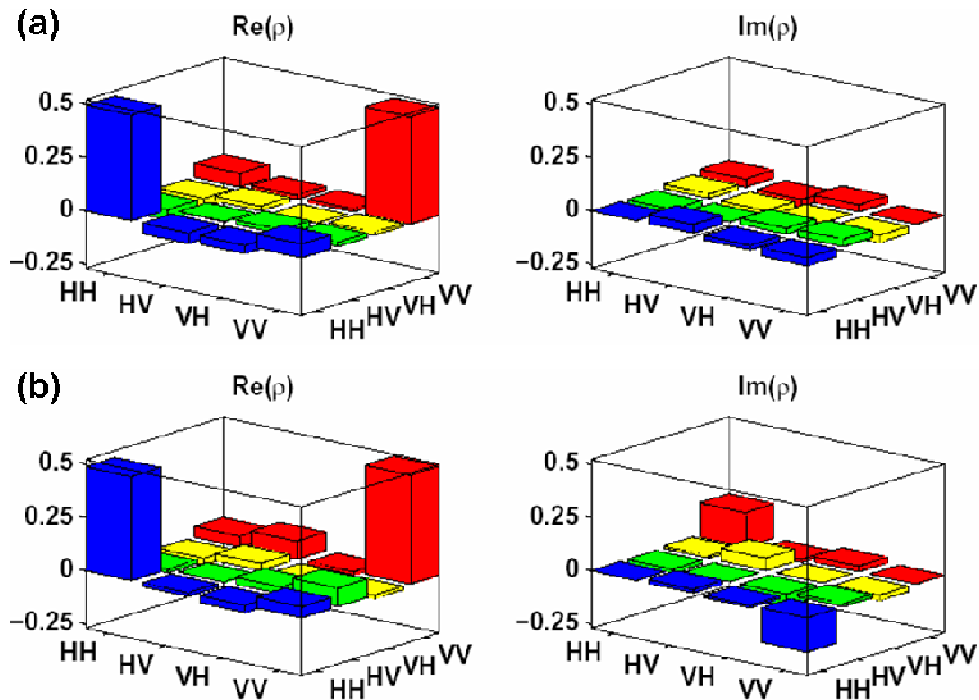


Fig. 17. Measured two-photon polarization density matrices. (a) No spectral filtering. (b) With spectral filtering. Left (right) – real (imaginary) part. The Peres-criterion negativity for the matrix shown in (a) [(b)] is  $0.03 \pm 0.04$  [ $0.18 \pm 0.05$ ].

### *Spin-blockaded radiative cascade*

We recently discovered a novel radiative cascade which initiates from a metastable spin blockaded biexcitonic state [70] rather than from the ground biexciton state. This cascade is an indirect one. The metastable biexciton state from which the cascade starts, is composed of two electrons in their ground singlet state and two holes, one in its ground state and the other in an excited state. The two holes can form either a spin-singlet or a spin-triplet. The singlet state can relax to the ground state without changing its spin. The triplet states cannot, and they are thus metastable, blockaded from thermalization into their ground singlet state by Pauli's exclusion principle. These metastable biexciton states radiatively decay to form a single exciton which

contains a hole in an excited state. This hole is now free to relax to its ground state, by the emission of a phonon, resulting in a ground-state exciton. The ground-state exciton then radiatively decays to the vacuum state. Consequently, this cascade involves the emission of three particles: two photons and one phonon. The intermediate non-radiative decay is fast ( $\sim 30$  ps [71]), and as shown below, preserves the exciton's spin. For a spin-preserving non-radiative decay, one expects all the 'which-path' information carried by the intermediate phonon to reside in its energy. Therefore, one may expect this cascade to be another example where spectral filtering would be effective in restoring entanglement. We found that this is not the case. We applied the same filtering scheme to the two types of radiative cascades, in the same quantum dot, and found that while for the ground-state biexciton cascade entanglement was restored, this was not the case for the spin-blockaded biexciton cascade. As discussed below, this is attributed to the "wrong" sign in the detuning of the two intermediate levels, combined with the fluctuating electrostatic environment ('spectral diffusion') [7].

The relevant levels diagram of a neutral QD is presented in Fig. 18a. The ground-state biexciton is marked by S (for Singlet), and the excited singlet biexciton is marked by  $S^*$ . The metastable biexciton states are marked by  $T_0$  and  $T_{\pm 3}$ . T stands for Triplet and the subscripts stand for the total- two holes' spin projection on the QD's growth direction. The triplet biexciton states are not split by the electron-hole exchange interaction since the total electronic spin is zero. High orders of the hole-hole exchange interaction can lower the  $T_{\pm 3}$  states in respect to the  $T_0$  state [72]. In our case however, the separation is smaller than the isotropic electron-hole exchange, which splits the dark and bright exciton states. The order of the  $T_0$  and  $T_{\pm 3}$  emission lines is thus the same as in the case of no hole-hole anisotropic exchange interaction (see Fig. 18a). We therefore neglect the contribution of these high orders to the hole-hole exchange in the following

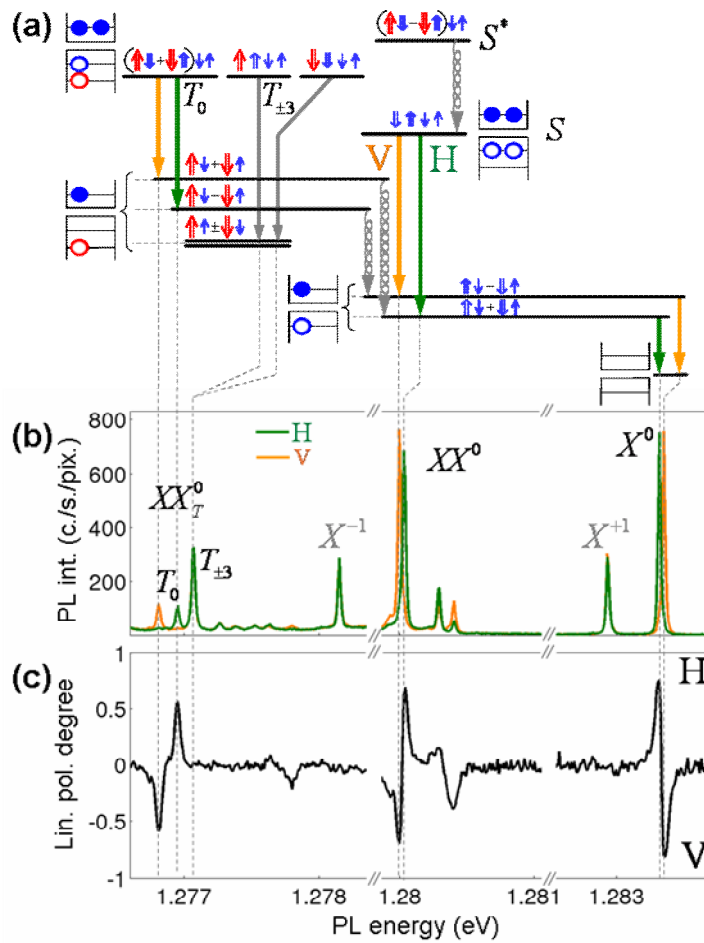


Fig. 18. (a) Energy levels diagram for excitons and biexcitons in a neutral QD. Single-carrier level occupations are given along side each many-carrier level. The spin wavefunctions are depicted above each level. The symbol  $\uparrow$  ( $\downarrow$ ) represents spin up (down) electron (hole). Short (long) symbols represent charge-carriers in the first (second) energy level. S ( $S^*$ ) indicates the ground (excited) biexciton hole-singlet state.  $T_0$  ( $T_{\pm 3}$ ) indicates the metastable spin-triplet biexciton state with z-axis spin projection of 0 ( $\pm 3$ ). The solid (curly) vertical arrows indicate spin preserving (non-) radiative transitions. Dark (light) gray arrows represent photon emission in horizontal - H (vertical - V) polarization. (b) Polarized PL spectra. H (V) in dark (light) gray. Spectral lines which are relevant to this work are marked and linked to the transitions in (a) by dashed lines. (c) Linear polarization spectrum. The value 1 (-1) means full H (V) polarization.

discussion. Recombinations from the  $T_{\pm 3}$  states lead to the optically inactive ('dark') exciton intermediate states (see the spectral line in Fig. 18b). Radiative decay does not proceed from these states and therefore they are not discussed here further [34]. The  $T_0$  biexciton state recombines to form one of two *excited* exciton states. As in the case of the ground-state exciton discussed above, these states are the symmetric and antisymmetric combinations of spin projection eigenstates. Here however, the energetic ordering between the symmetric and antisymmetric combinations is the opposite of that between the ground-state exciton states. This is due to the opposite sign of the relevant anisotropic electron-hole exchange term, as seen in table 1 above. It can be understood by noting that the quadrupole moment of the  $p_x$ -type spatial wavefunction of the excited hole, is opposite in respect to that the  $s$ -type ground-state hole wavefunction.

Another difference between the  $T_0$  and  $S$  biexciton cascades arises in the polarization selection rules for optical recombination of the biexciton. Due to the reversed spin-exchange symmetry of the  $T_0$  biexciton in respect to that of the  $S$  biexciton, the polarization selection rules are reversed: while in the  $S$  biexciton case horizontal polarization leads to the symmetric combination, in the  $T_0$  case it leads to the antisymmetric combination. This is similar to the case of the doubly-charged exciton discussed above, where the selection rules depend on whether the final state belongs to a spin singlet or a spin triplet. Nevertheless, the order of polarizations of the emission line's components will be the same for the two biexcitons. This is because the difference in the selection rules is compensated by the difference in the ordering of the levels. As seen in the polarized PL spectra presented in Fig. 18b, and in the corresponding spectrum of linear polarization degree shown in Fig. 18c, this is indeed the case.

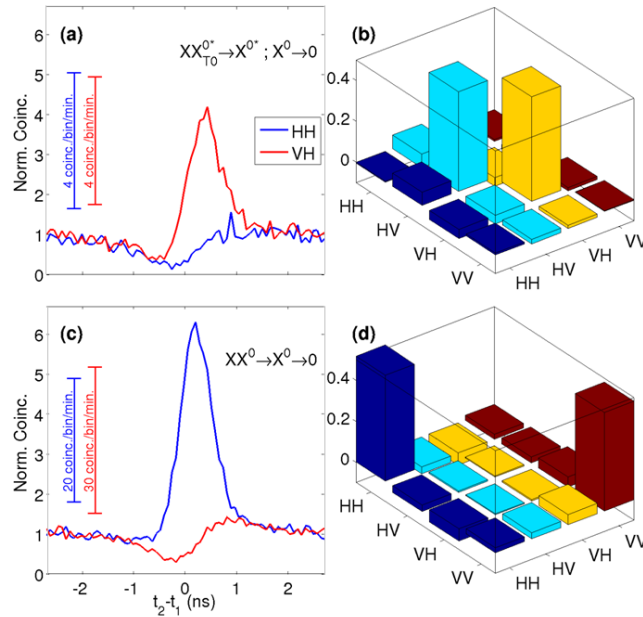


Fig. 19. (a), (c) Measured intensity correlation functions for the spin-blockaded and ground-state biexciton cascades, respectively. Dark (light) gray line represents the correlation in co- (cross-) linear polarizations. The coincidence rates are indicated by the scale-bars in units of coincidences per time bin (80 ps) per minute. (b), (d) Real parts of the two-photon polarization density matrices measured for the spin-blockaded and ground-state biexciton cascades, respectively.

The hole of the excited exciton states is not spin-blockaded, and it quickly decays (non-radiatively) to its ground state, *while preserving its spin*. Therefore, horizontally (H) polarized  $T_0$  biexciton recombination will be followed by vertically (V) polarized exciton recombination (see Fig. 18a). This leads to correlated *cross*-linearly polarized photons, unlike the correlated co-linearly polarized photons emitted in the S biexciton cascade.

In Fig. 19a (Fig. 19c) we present measured time resolved intensity correlation functions between the  $T_0$  (S) biexciton line and the exciton line, in both co- (dark-gray) and cross- (light gray) linear polarizations. It is clearly seen that while for the cascade starting from the S biexciton, the

emission of the exciton is “bunched” for co-linear polarizations and “anti-bunched” for cross-linear polarizations, the opposite happens for the cascade starting from the  $T_0$  biexciton. This confirms that there is no change in the spin-configuration during the decay of the hole.

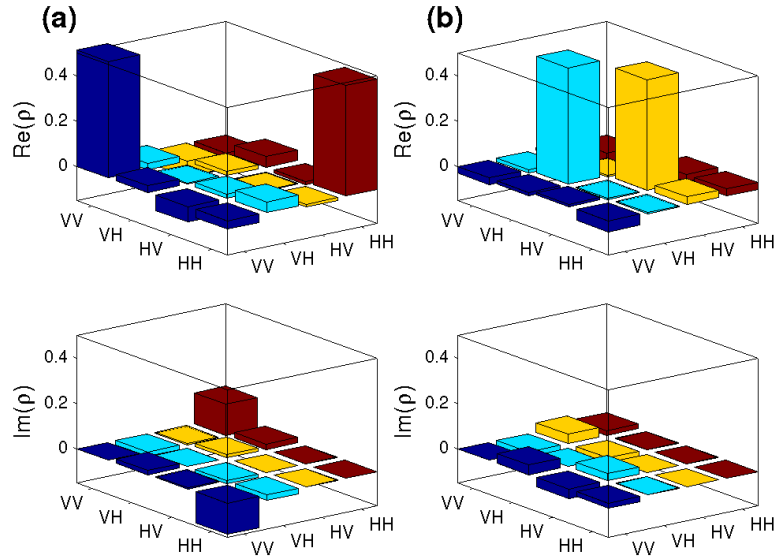


Fig. 20. (a), (b) Measured two-photon polarization density matrices for the ground-state (S) and spin-blockaded ( $T_0$ ) biexciton cascades, respectively, as obtained with spectral filtering. Real (imaginary) parts are shown in the top (bottom) panels. The Peres-criterion negativity for the matrix in (a) [(b)] is  $0.15 \pm 0.03$  [ $0.05 \pm 0.1$ ].

In addition, we performed full polarization tomography for both cascades, both with and without spectral filtering. The resulting two-photon polarization density matrices for the case of no filtering are presented in Fig. 19b (Fig. 19d) for the  $T_0$  (S) biexciton cascade. Since the imaginary parts of the matrices were zero to within the measurement uncertainty, only the real parts are displayed. In Fig. 20 we present the density matrices obtained for the case of spectral filtering. While entanglement could be restored for photon pairs emitted from the S biexciton cascade (Fig. 20a), no such restoration could be achieved for the  $T_0$  cascade (Fig. 20b). The

differences between the two cases are discussed below.

Fig. 21a shows the cascade initiated by the ground state of a biexciton in an ideal, symmetric QD. In this case, the two exciton energy levels are degenerate, and emitted photon pairs will be entangled [55]. Fig. 21b shows the case of the ground-state biexciton cascade in an asymmetric QD, in which the exciton levels are split by an energy  $\delta$ . Here, spectral filtering (crosshatched rectangle) is necessary for the emitted photons to be entangled. Fig. 21c shows a schematic plot of the two-photon probability distribution. The x- (y-) axis represents the energy of the exciton (biexciton) photon. The dark-gray spots show the regions of high emission probability. Their size and shape are determined by the radiative width of the exciton ( $\gamma_x$ ) and biexciton ( $\gamma_{xx}$ ) lines. The emission in these regions is dominated by un-entangled photon pairs. The energies of the two photons are related by total energy conservation: if the first photon has high energy, the second one will have low energy, and vice-versa. This puts the two dark-gray spots on a line parallel to the (1,-1) direction. The cross hatched rectangle represents an optimal spectral filter for entanglement restoration. It is  $\gamma_x$  by  $\gamma_{xx}$  in size. It rejects most of the un-entangled photon-pairs while it keeps a measurable fraction of the entangled pairs, which lie mostly between the two dark gray spots, on the connecting line. The degree of entanglement within the transmitted photon pairs is thus increased. A smaller filter would yield higher degree of entanglement, but will transmit considerably less photons. Due to random fluctuations in the electrostatic environment of the QD, the energies of the spectral lines fluctuate with time.

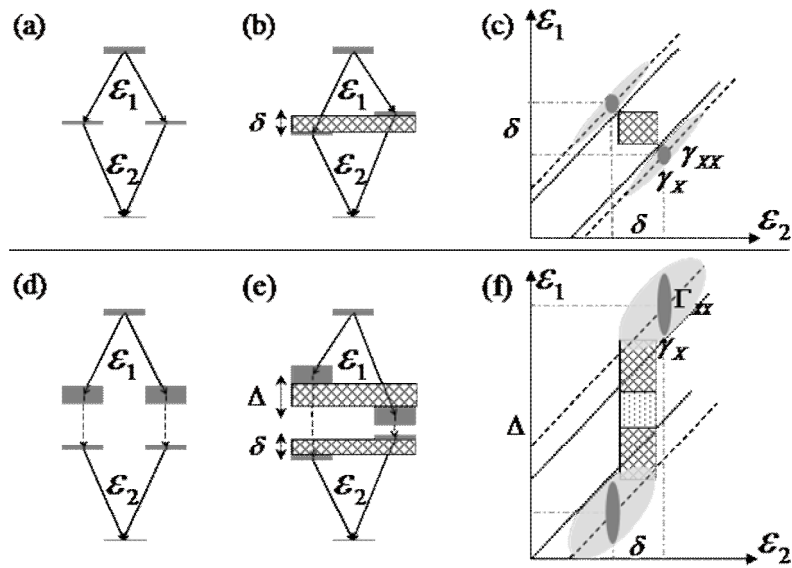


Fig. 21. (a) Ideal direct cascade. The widths of the levels represent their decay rate. (b) Ground state biexciton cascade in an anisotropic QD. (c) Schematic two-photon probability distribution. Dark gray - high probability areas. Cross-hatched - spectral filter. Light gray - inhomogeneous broadening due to spectral diffusion. (d)-(f) Same as (a)-(c) (respectively), for an indirect cascade. In (e) and (f) only the case of splittings in opposite directions is shown. The dotted rectangle in (f) is an example for a filter not penetrated by the high-probability areas for any amount of spectral diffusion.

This “spectral diffusion” happens on timescales much longer than the radiative recombination time of the exciton. The random electric field is thus quasi-static. Since all spectral lines experience almost the same shift in a given static electric field [44, 73] the energies of the exciton and biexciton lines will fluctuate in a correlated manner. The dark-gray spots of Fig 21c will thus randomly move along the dashed lines parallel to the (1,1) direction, as shown in the figure by the light-gray areas. As these areas are outside the filter, spectral diffusion does not interfere with the entanglement restoration. Indeed, as was discussed above (Fig. 20a),

entanglement can be restored by spectral filtering for the ground state biexciton cascade.

The situation is different for an indirect radiative cascade. Figures 21d-21f present the case of the spinblockaded biexciton radiative cascade. Here there is a fast, non-radiative (phononic) decay of the hole from its first-excited state to its ground state between the biexciton and exciton radiative recombinations. Fig. 21d shows the ideal case where the excited and ground exciton states are each two fold degenerate. The short lifetime of the excited exciton states is represented by the large width of the energy levels. Since the spin of the exciton is conserved during the intermediate stage, and since the spatial parts of the exciton wavefunctions are identical for both decay paths, the emitted phonon does not carry any ‘which path’ information beyond its energy. In this case one expects that appropriate filtering of the photon energies will restore the which-path ambiguity, resulting in entanglement of the polarization state of the photons. Fig. 21e shows the case of an asymmetric QD. The degeneracy is lifted for both ground and excited exciton states, in opposite manners. Due to the opposite splittings, the energies of the two photons are positively rather than negatively correlated. This is shown in Fig. 21f, where the dark-gray spots again represent the regions of high probability. Their elongated shape is due to the larger width of the biexciton photon, which comes from the fast decay of its final state. Spectral diffusion will still shift these regions along the (1,1) direction, as shown by light gray. The analog of the optimal filter for this case is shown by the cross hatched rectangle. It is  $\Delta - \Gamma_{xx}$  by  $\delta - \gamma_x$  where  $\Delta$  is the excited exciton splitting (in absolute value) and  $\Gamma_{xx}$  is the width of the spin-blockaded biexciton transition. As in the previous case, such a filter excludes the dark-gray spots. However, it is not immune to spectral diffusion, as shown by the overlap of the cross hatched rectangle and the light gray areas. Indeed, as shown in Fig. 20b, no entanglement could be detected even when this filter was applied. Further decreasing the filter width may solve the

spectral diffusion problem, but then the photon pair collection rate would drastically decrease.

We note that if the ground and excited exciton states would have split to the same direction, the situation would have been similar to that described in Fig. 21c, and entanglement restoration by spectral filtering would not have been affected by spectral diffusion. A quantitative condition for spectral filtering to effectively erase the which-path information can be formulated by inspecting Figs. 21c and 21f. Note first that spectral diffusion leads to motion of the dark gray spots along the (1,1) direction. Spectral filtering works if during this motion the spots stay strictly outside the filter area. The width of the filter that satisfies this condition is determined by looking at the projection of the filter on the orthogonal direction to the motion of the spots: the (1,-1) direction. Let  $f > 0$  ( $F > 0$ ) be the filter width for the exciton (biexciton) photon spectral line. The filter's projection on the (1,-1) direction is given by  $(f + F)/\sqrt{2}$ . The projection of the line connecting the centers of the two dark-gray spots on the (1,-1) direction is given by  $|\Delta \pm \delta|/\sqrt{2}$  where the plus sign is for Fig. 21c and the minus sign is for Fig. 21f. For avoiding overlap one thus must have  $f + F \leq |\Delta \pm \delta|$ . The case of a minus sign forces narrow filter widths, which makes spectral filtering ineffective. Taking into account the widths of the lines (the sizes of the dark-gray spots), leads to an even stronger constraint,

$$f + F \leq |\Delta \pm \delta| - (\Gamma_{xx} + \gamma_x) \quad (1.40)$$

where  $\Gamma_{xx}$  refers also to  $\gamma_{xx}$  as appropriate. This explains why spectral filtering was ineffective for the spin blockaded biexciton cascade.

*Radiative cascades in singly charged quantum dots*

We recently demonstrated [71] that radiative cascades occur also when the QD is charged. In this case, the intermediate, charged exciton level maybe metastable, spin-blockaded from thermal relaxation. In the following we present and discuss measurements performed on a positively charged QD.

The energy levels of a positively charged QD [37, 38] containing up to three heavy holes and two electrons are schematically described in Fig. 22a. The figure presents also the relevant radiative and nonradiative total-spin conserving transitions between these levels. The two photon radiative cascades start from the ground level of the three heavy holes and two electrons state. The unpaired hole's spin projection along the growth axis determines the total spin of the two Kramers' degenerate states (for simplicity only one state is drawn in Fig. 22a). Radiative recombination of first level e-h pair leaves three unpaired charge carriers within the QD. There are 8 possible different spin configurations for the remaining carriers. These configurations form 4 energy levels of Kramers' pairs [37, 38]. The three lowest levels are those in which the two unpaired holes are in spin-triplet states. Those states are separated from the highest energy level in which the holes are in a singlet spin state by the hole-hole isotropic exchange interaction, which is significantly stronger than the e-h exchange interaction. The later removes the degeneracy between the triplet states as shown in Fig. 22a. The lowest triplet level cannot be reached optically. The optical transitions into the other levels are optically allowed. The circular polarizations of the emitted photons are indicated in the figure. They depend on the spins of the annihilated electron hole pair. The measured emission contains also linear components (see Fig. 22c), due to the anisotropic e-h exchange interaction [37, 38].

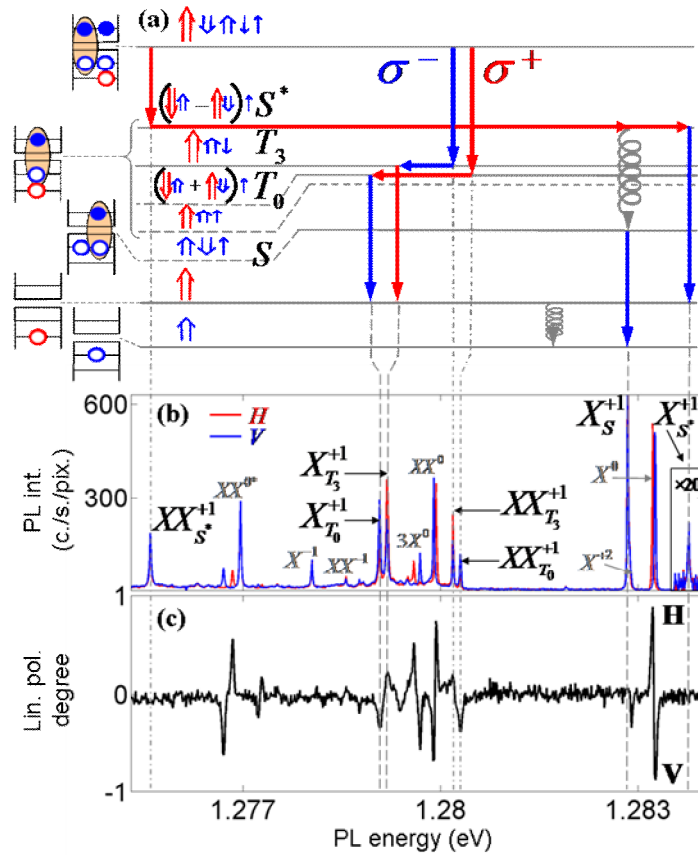


Fig. 22. (a) Schematic description of the energy levels of a singly positively charged QD.

Vertical (curly) arrows indicate radiative (nonradiative) transitions between these levels. State occupation and spin wavefunctions are described to the left of each level where  $\uparrow$  ( $\downarrow$ ) represents an electron (hole) with spin up (down). A short blue (long red) arrow represents a carrier in its first (second) level. S (T) stands for two holes' singlet (triplet) state and 0 (3) for  $S_z = 0$  ( $S_z = \pm 3$ ) total holes' pseudo-spin projection on the QD growth direction. The excited state singlet is indicated by  $S^*$ . Only one out of two (Kramers') degenerate states is described. (b) Measured PL spectrum on which the actual transitions are identified. Transitions which are not discussed here are marked by gray letters. (c) Measured degree of linear polarization spectrum, along the in-plane symmetry axes of the QD. Positive (negative) value represents polarization along the QD's major (minor) axis.

The relaxation proceeds by radiative recombination of the remaining first level e-h pair, leaving thus only one hole in its second level. The hole can then quickly relax non-radiatively to its ground level. There is a fundamental difference between the singlet and triplet intermediate states. While in the later, due to Pauli's exclusion principle, radiative recombination must occur before the excited hole can relax to its ground state (resulting in two "direct" cascades), in the former non-radiative relaxation of the excited hole state may occur prior to the radiative recombination (resulting in one "direct" and one "indirect" cascade).

In Fig. 22b we present the spectrum measured under non-resonant cw excitation with 1  $\mu$ W of HeNe laser light (1.96 eV). The corresponding degree of linear polarization is presented in Fig. 22c. The spectral lines participating in the radiative cascades described in Fig. 22a are clearly identified spectrally in the single QD PL and linear polarization spectra.

In Fig. 23 we present the measured and calculated intensity correlation functions for photon pairs emitted in the four spin-conserving radiative cascades outlined in Fig. 22a. The measured data clearly reveal the sequence of the radiative events, reassuring the interpretations of Fig. 22.

In Fig. 24 we present measured and calculated intensity correlation functions between different radiative cascades. Since spin blockade prevents the relaxation of the second level hole to its first level, they provide an estimate for the rate by which the holes' spin scatters [73]. In Fig. 24a and 24c we probe possible transitions from the singlet intermediate state  $S^*$  to the triplet  $T_0$  and  $T_{\pm 3}$  intermediate states, respectively.

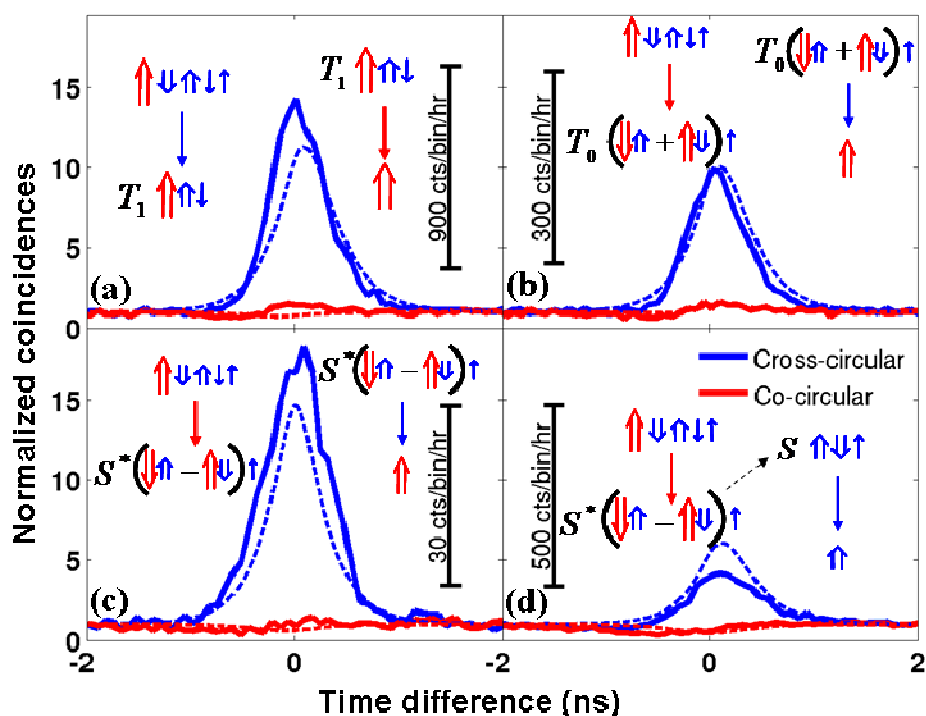


Fig. 23. Measured and calculated time resolved, polarization sensitive intensity correlation functions, for the 4 radiative cascades described in Fig. 22. The states involved in the first (second) photon emission are illustrated to the left (right) side of each panel. All symbols and labels are as in Fig. 22. Solid Blue (red) line stands for measured cross- (co-) circularly polarized photons. Dashed lines represent the corresponding calculated functions. The bar presents the acquisition rate in coincidences per time bin (80 ps) per hour.

In Figs. 24b and 24d we probe possible transitions from the triplet  $T_0$  and  $T_{\pm 3}$  intermediate states, respectively, to the singlet ground state  $S$ . Assuming that relaxation from the intermediate triplet states to the ground singlet states must be preceded by transition to the intermediate singlet states, these measurements provide quantitative estimation for the reverse of the processes described in 24a and 24c. From the measured data in Fig. 24 one clearly notes that transition between the two holes' singlet state to the  $T_{\pm 3}$  triplet state (Fig. 24c) and vice versa (Fig. 24d) are

forbidden (within the radiative lifetime), while transitions between the singlet and the  $T_0$  triplet states (Fig. 24a) and vice versa (Fig. 24b) are partially allowed.

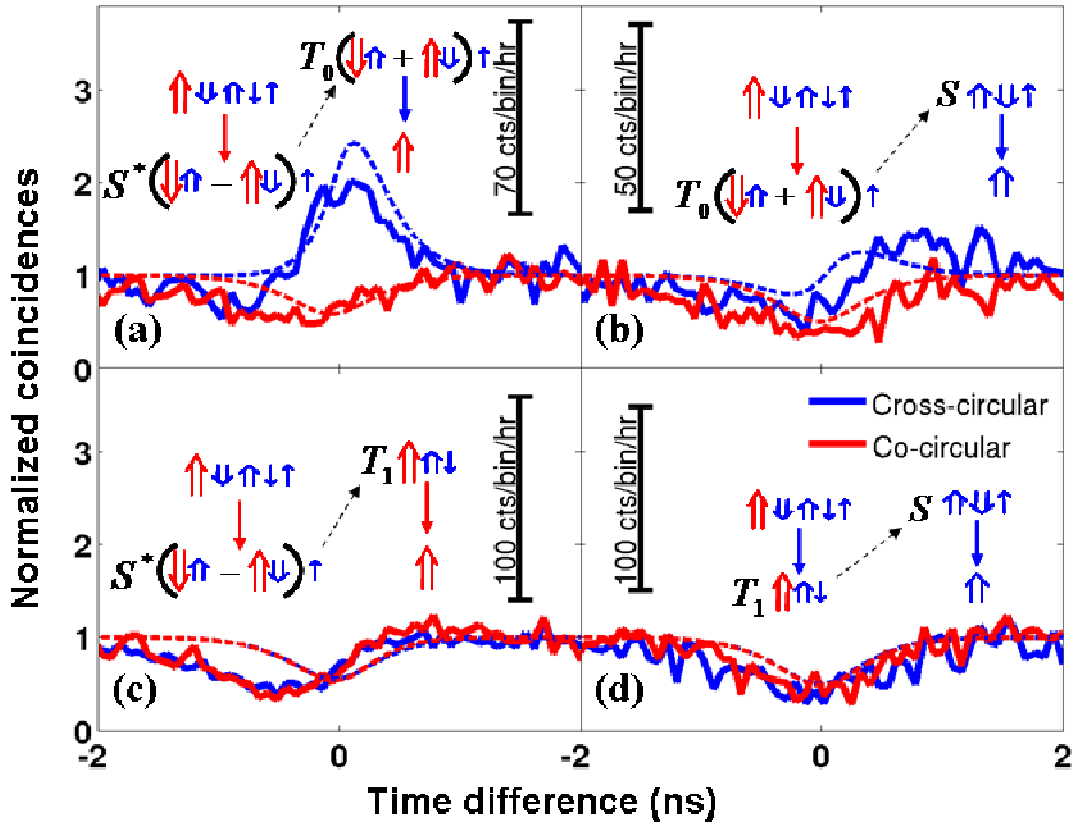


Fig. 24. Measured and calculated time resolved, polarization sensitive intensity correlation functions, across the radiative cascades. (a) [(c)] Correlations between the singlet biexciton transition and the exciton transition from the  $T_0$ , [ $T_3$ ] state. (b) [(d)] Correlations between the  $T_0$ , [ $T_3$ ] biexciton transition and the ground  $X+1$  exciton transition. All symbols and labels are as in Fig. 22. The meanings of all line types and colors are as in Fig. 23.

This means that the holes spin projection on the QD's growth axis is conserved during the relaxation while their in-plane spin projection scatters [73]. The difference between the scattering rates from the singlet to triplet state and that from the triplet to singlet is due to the

energy difference between these two states ( $\sim 4$  meV), which is much larger than the ambient thermal energy ( $\sim 0.5$  meV).

In order to calculate the expected correlation functions and to compare them to the measured ones, we used a classical rate equation model. In this model we include all the states as described in Fig. 22(a), together with their Kramers conjugates. In addition, we include four more states representing charged multi-excitons up to 6 e-h pairs [53]. There are clear spectral evidences for processes in which the QD changes its charge state and becomes neutral due to optical depletion [74, 75] (see Fig. 22b). These observations are considered in our model by introducing one additional state which represents a neutral QD. The transition rates between the states include radiative rate ( $\gamma_r = 1.25ns^{-1}$  deduced directly from the PL decay of the exciton lines) and non-radiative spin-conserving rate ( $\Gamma_{S^* \rightarrow S} = 35\gamma_r$ , deduced from the intensity ratios of the  $S^*$  and the  $S$  PL lines). We also include the rate for optical generation of e-h pairs ( $G_e = 1\gamma_r$  forced by equating between the emission intensities of the biexciton and exciton spectral lines), and the optical depletion, and recharging rates ( $G_D = 4\gamma_r$  and  $G_C = 0.1\gamma_r$  as deduced from the relevant line intensity ratios, and correlation measurements between the neutral and charged exciton). The data clearly show that hole spin scattering rates, ( $\Gamma_{S \rightleftharpoons T_3}$ ) which do not conserve the spin projection on the QD's growth axis, are vanishingly small. Therefore we set them to 0. In order to account for the observed correlations between singlet ( $S$ ) and  $T_0$  states, Fig. 3, we fitted in-plane scattering rates [73]  $\Gamma_{T_0 \rightarrow S} = 0.6\gamma_r$  and  $\Gamma_{S^* \rightarrow T_0} = 10\gamma_r$  (such processes still conserve the projection of the total spin along the growth axis). The ratio between these rates simply gives the temperature of the optically excited QD ( $\sim 19K$ ).

\The anisotropic EHEI mixes the  $T_0$  and  $T_{\pm 3}$  states [37, 38]. This makes the natural polarizations

of the relevant transitions elliptical rather than circular. The mixing degree is obtained from the measured degree of linear polarization of the biexciton transitions [38]. Our model considers this mixing as well. It explains the non-zero correlations in co-circular polarizations.

The two inplane hole's spin scattering rates that we fitted describe very well the 16 measured intensity correlation functions. The calculated functions (convoluted with the system response) are presented in Fig. 23 and Fig. 24 by dashed lines.

Over all, we identified 3 direct and one indirect radiative cascades in singly charged QDs and demonstrated unambiguous correlations between the polarizations of the emitted photons and the spin of the remaining charge carrier. Our correlation measurements show that while holes' spin-projection conserving scattering rates are a few times faster than the radiative rates, spin-projection non-conserving rates are vanishingly small.

### ***Summary***

We discussed and reviewed photoluminescence spectroscopy from single semiconductor quantum dots in general, and radiative cascades from these nanostructures, in particular. For understanding in details the available rich experimental data we developed a theoretical many interacting carrier model. Our model, though relatively simple, describes very well the measured polarization sensitive photoluminescence spectra. In particular, we were able to explain linear and circular polarization memory in quasi-resonant optical excitation of the quantum dots. We concluded this chapter with quantitative analysis of polarization sensitive intensity correlation measurements of various biexciton-exciton radiative cascades in neutral and charged quantum dots. Emission of polarization entangled pairs of photons in these cascades was reviewed with strong emphasis on spectral filtering as a tool for distilling entanglement.

We believe that the insights and findings that we reviewed here be useful for future developments of semiconductor quantum dots as an important tool for quantum information processing technologies.

### **References**

- [1] M. A. Kastner, Artificial atoms. *Phys. Today* **46**, 24 (1993).
- [2] R. C. Ashoori, Electrons in artificial atoms. *Nature* **379**, 413 (1996).
- [3] D. Gammon, Semiconductor physics: Electrons in artificial atoms. *Nature* **405**, 899 (2000).
- [4] P. J. Carson, G. F. Strouse, P. Michler, A. Imamoglu, M. D. Mason, and S. K. Buratto, Quantum correlation among photons from a single quantum dot at room temperature. *Nature*, **406**, 968 (2000).
- [5] E. Hu, P. Michler, A. Kiraz, C. Becher, W. V. Schoenfeld, P. M. Petroff, L. Zhang, and A. Imamoglu, Quantum correlation among photons from a single quantum dot at room temperature. *Science*, **290**, 2282 (2000).
- [6] C. Santori, M. Pelton, G. Solomon, Y. Dalem, and Y. Yamamoto, Triggered single photons from a quantum dot. *Phys. Rev. Lett.* **86**, 1502 (2001).
- [7] N. Akopian, N. H. Lindner, E. Poem, Y. Berlatzky, J. Avron, D. Gershoni, B. D. Gerardot, and P. M. Petroff, Entangled photon pairs from semiconductor quantum dots. *Phys. Rev. Lett.* **96**, 130501 (2006).
- [8] R. Hafenbrak, S. M. Ulrich, P. Michler, L. Wang, A. Rastelli, and O. G. Schmidt, Triggered polarization-entangled photon pairs from a single quantum dot up to 30 K. *New J. Phys.* **9**, 315 (2007).

- [9] D. Loss and D. P. DiVincenzo, Quantum computation with quantum dots. *Phys. Rev. A*, **57** 120 (1998).
- [10] C. H. Bennett and G. Brassard, Quantum cryptography: Public key distribution and coin tossing. In *Proc. IEEE Int. Conf. Comput. Syst. Signal Process.* (Bangalore, India, Dec. 1984).
- [11] B. Lounis and W. E. Moerner, Single photons on demand from a single molecule at room temperature. *Nature* **407** 491 (2000).
- [12] H. Drexler, D. Leonard, W. Henson, J. P. Kotthaus, and P. M. Petroff, Spectroscopy of quantum levels in charge-tunable InGaAs quantum dots. *Phys. Rev. Lett.* **73**, 2252 (1994).
- [13] A. Szabo and N. S. Ostlund. Modern quantum chemistry: Introduction to advanced electronic structure theory. Dover, Minoela, N.Y., 1996.
- [14] L. Fetter and J. D. Walecka, Quantum theory of many particle systems. McGraw-Hill, New-York, 1971.
- [15] A. Barenco and M. A. Dupertuis, Quantum many-body states of excitons in a small quantum dot. *Phys. Rev. B* **52**, 2766 (1995).
- [16] E. L. Ivchenko and G. E. Pikus. Super lattices and other hetero structures, volume 110 of Springer series in solid state sciences. Springer Verlag, Berlin, 1997.
- [17] T. Takagahara, Theory of exciton doublet structures and polarization relaxation in single quantum dots. *Phys. Rev. B* **62**, 16840 (2000).
- [18] M. Bayer, G. Ortner, O. Stern, A. Kuther, A. A. Gorbunov, A. Forchel, P. Hawrylak, S. Fafard, K. Hinzer, T. L. Reinecke, S. N. Walck, J. P. Reithmaier, F. Klopff, and F. Schafer, Fine structure of neutral and charged excitons in self assembled In(Ga)As/(Al)GaAs quantum dots. *Phys. Rev. B* **65**, 195315 (2002).

- [19] L. W. Wang, A. J. Williamson, and A. Zunger, Theoretical interpretation of the experimental electronic structure of lens shaped self assembled InAs/GaAs quantum dots. *Phys. Rev. B*, **62**, 12963 (2000).
- [20] S. Lee, L. Jönsson, J. W. Wilkins, G. W. Bryant, and G. Klimeck, Electron-hole correlations in semiconductor quantum dots with tight-binding wave functions. *Phys. Rev. B* **63**, 195318 (2001).
- [21] M. Zielinski, M. Korkusiński, and P. Hawrylak, Atomistic tight-binding theory of multiexciton complexes in a self-assembled InAs quantum dot. *Phys. Rev. B* **81**, 085301 (2010).
- [22] D. Gershoni, Eigen function expansion method for solving the quantum wire problem: Formulation. *Phys. Rev. B* **43**, 4011 (1991).
- [23] M. Grundmann, O. Stier, and D. Bimberg, InAs/GaAs pyramidal quantum dots: Strain distribution, optical phonons and electronic structure. *Phys. Rev. B* **52**, 11969 (1995).
- [24] H. Jiang and J. Singh. Strain distribution and electronic spectra of InAs/GaAs self assembled quantum dots: An eight band study. *Phys. Rev. B* **56**, 4696 (1997).
- [25] C. Pryor, Eight-band calculations of strained InAs/GaAs quantum dots compared with one-, four-, and six-band approximations. *Phys. Rev. B* **57**, 7190 (1998).
- [26] A. Kumar, S. E. Laux, and F. Stern, Electron states in a GaAs quantum dot in a magnetic field. *Phys. Rev. B* **42**, 5166 (1990).
- [27] U. Merkt, J. Huser, and M. Wagner, Energy spectra of two electrons in a harmonic quantum dot. *Phys. Rev. B* **43**, 7320 (1991).
- [28] E. Poem, J. Shemesh, I. Marderfeld, D. Galushko, N. Akopian, D. Gershoni, B. D. Gerardot, A. Badolato, and P. M. Petroff, Polarization sensitive spectroscopy of charged

- quantum dots. *Phys. Rev. B* **76**, 235304 (2007).
- [29] H. A. Kramers, General theory of paramagnetic rotation in crystals. *Proc. Acad. Sci. Amsterdam* **33**, 959 (1930).
- [30] V. Mlinar and A. Zunger, Effect of atomic-scale randomness on the optical polarization of semiconductor quantum dots. *Phys. Rev. B* **79**, 115416 (2009).
- [31] D. M. Bruls, J. W. A. M. Vugs, P. M. Koenraad, H. W. M. Salemink, J. H. Wolter, M. Hopkinson, M. S. Skolnick, Fei Long, and S. P. A. Gill, Determination of the shape and indium distribution of low-growth-rate InAs quantum dots by cross-sectional scanning tunneling microscopy. *Appl. Phys. Lett.* **81**, 1708 (2002).
- [32] K. V. Kavokin, Symmetry of anisotropic exchange interactions in semiconductor nanostructures. *Phys. Rev. B*, **69**, 075302 (2004).
- [33] Cohen-Tannoudji, B. Diu, and F. Laloe, Quantum Mechanics. Wiley-Interscience, New York, 1977.
- [34] E. Poem, Y. Kodriano, N. H. Lindner, C. Tradonsky, B. D. Gerardot, P. M. Petroff, and D. Gershoni, Accessing the dark exciton with light. *Nature Phys.* **6**, 993 (2010).
- [35] H. Henry and K. Nassau, Lifetimes of bound excitons in CdS. *Phys. Rev. B* **1**, 1628 (1970).
- [36] S. Rodt, A. Schliwa, K. Pötschke, F. Guffarth, and D. Bimberg, Correlation of structural and few-particle properties of self-organized InAs/GaAs quantum dots. *Phys. Rev. B* **71**, 155325 (2005).
- [37] K. V. Kavokin, Fine structure of the quantum-dot trion. *Phys. Stat. Sol. (a)* **195**, 592 (2003).
- [38] I. A. Akimov, K. V. Kavokin, A. Hundt, and F. Henneberger, Electron-hole exchange

- interaction in a negatively charged quantum dot. *Phys. Rev. B* **71**, 075326 (2005).
- [39] B. Urbaszek, R. J. Warburton, K. Karrai, B. D. Gerardot, P. M. Petroff, and J. M. Garcia, Fine Structure of Highly Charged Excitons in Semiconductor Quantum Dots. *Phys. Rev. Lett.* **90**, 247403 (2003).
- [40] E. Dekel, D. V. Regelman, D. Gershoni, E. Ehrenfreund, W. V. Schoenfeld, and P. M. Petroff, Cascade evolution and radiative recombination of quantum dot multiexcitons studied by time-resolved spectroscopy. *Phys. Rev. B* **62**, 11038 (2000).
- [41] G. Ramon, U. Mizrahi, N. Akopian, S. Braitbart, D. Gershoni, T. L. Reinecke, B. D. Gerardot, and P. M. Petroff, Emission characteristics of quantum dots in planar microcavities. *Phys. Rev. B* **73**, 205330 (2006).
- [42] R. I. Dzhioev, K. V. Kavokin, V. L. Korenev, M. V. Lazarev, B. Ya. Meltser, M. N. Stepanova, B. P. Zakharchenya, D. Gammon, and D. S. Katzer, Low- temperature spin relaxation in n-type GaAs. *Phys. Rev. B* **66**, 245204 (2002).
- [43] J. Hilton and C. L. Tang, Optical Orientation and Femtosecond Relaxation of Spin-Polarized Holes in GaAs. *Phys. Rev. Lett.* **89**, 146601 (2002).
- [44] M. E. Ware, E. A. Stinaff, D. Gammon, M. F. Doty, A. S. Bracker, D. Gershoni, V. L. Korenev, Ş. C. Bădescu, Y. Lyanda-Geller, and T. L. Reinecke, Polarized fine structure in the photoluminescence excitation spectrum of a negatively charged quantum dot. *Phys. Rev. Lett.* **95**, 177403 (2005).
- [45] D. Heiss, M. Kroutvar, J. J. Finley, G. Abstreiter, Progress towards single spin optoelectronics using quantum dot nanostructures. *Solid State Commun.* **135**, 591 (2005).
- [46] E. Dekel, D. V. Regelman, D. Gershoni, E. Ehrenfreund, W. V. Schoenfeld, and P.M. Petroff, Radiative lifetimes of single excitons in semiconductor quantum dots -

- manifestation of the spatial coherence effect. *Solid State Commun.* **117**, 395 (2001).
- [47] V. K. Kalevich, I. A. Merkulov, A. Yu. Shiryaev, K. V. Kavokin, M. Ikezawa, T. Okuno, P. N. Brunkov, A. E. Zhukov, V. M. Ustinov, and Y. Masumoto, Optical spin polarization and exchange interaction in doubly charged InAs self-assembled quantum dots. *Phys. Rev. B* **72**, 045325 (2005).
- [48] D. Gammon, E. S. Snow, B. V. Shanabrook, D. S. Katzer, and D. Park, Fine structure splitting in the optical spectra of single GaAs quantum dots. *Phys. Rev. Lett.* **76**, 3005 (1996).
- [49] M. Paillard, X. Marie, P. Renucci, T. Amand, A. Jbeli, and J.-M. Gérard, Spin relaxation quenching in semiconductor quantum dots. *Phys. Rev. Lett.* **86**, 1634 (2001).
- [50] I. Favero, G. Cassabois, C. Voisin, C. Delalande, Ph. Roussignol, R. Ferreira, C. Couteau, J. P. Poizat, and J.-M. Gérard, Giant optical anisotropy in a single InAs quantum dot in a very dilute quantum-dot ensemble. *Phys. Rev. B* **71**, 233304 (2005).
- [51] R. I. Dzhioev, B. P. Zakharchenya, E. L. Ivchenko, V. L. Korenev, Yu. G. Kusraev, N. N. Ledentsov, V. M. Ustinov, A. E. Zhukov, and A. F. Tsatsulnikov, Fine structure of excitonic levels in quantum dots. *J. Exp. Theor. Phys. Lett.* **65**, 804 (1997).
- [52] R. Hanbury Brown and R.Q. Twiss, A Test of a New Type of Stellar Interferometer on Sirius. *Nature* **178**, 1046 (1956).
- [53] D. V. Regelman, U. Mizrahi, D. Gershoni, E. Ehrenfreund, W. V. Schoenfeld, and P. M. Petroff, Semiconductor quantum dot: A quantum light source of multicolor photons with tunable statistics. *Phys. Rev. Lett.* **87**, 257401 (2001).
- [54] H.-P. Breuer and F. Petruccione, The theory of open quantum systems. Oxford University Press, 2002.

- [55] O. Benson, C. Santori, M. Pelton, and Y. Yamamoto, Regulated and entangled photons from a single quantum dot. *Phys. Rev. Lett.* **84**, 2513 (2000).
- [56] E. Moreau, I. Robert, L. Manin, V. Thierry-Mieg, J.-M. Gérard, and I. Abram, Quantum cascade of photons in semiconductor quantum dots. *Phys. Rev. Lett.* **87**, 183601 (2001).
- [57] C. Santori, D. Fattal, M. Pelton, G. S. Solomon, and Y. Yamamoto, Polarization-correlated photon pairs from a single quantum dot. *Phys. Rev. B* **66**, 045308 (2002).
- [58] D. Gerardot, S. Seidl, P. A. Dalgarno, R. J. Warburton, D. Granados, J. M. Garcia, K. Kowalik, O. Krebs, K. Karrai, A. Badolato, and P. M. Petroff, Manipulating exciton fine structure in quantum dots with a lateral electric field. *Appl. Phys. Lett.* **90**, 041101 (2007).
- [59] A. Muller, W. Fang, J. Lawall, and G. S. Solomon, Creating Polarization-Entangled Photon Pairs from a Semiconductor Quantum Dot Using the Optical Stark Effect. *Phys. Rev. Lett.* **103**, 217402 (2009).
- [60] R. M. Stevenson, R. J. Young, P. See, D. G. Gevaux, K. Cooper, P. Atkinson, I. Farrer, D. A. Ritchie, and A. J. Shields, Magnetic-field-induced reduction of the exciton polarization splitting in InAs quantum dots. *Phys. Rev. B* **73**, 033306 (2006).
- [61] S. Seidl, M. Kroner, A. Högele, K. Karrai, R. J. Warburton, A. Badolato, and P. M. Petroff, Effect of uniaxial stress on excitons in a self-assembled quantum dot. *Appl. Phys. Lett.* **88**, 203113 (2006).
- [62] R. J. Young, R. M. Stevenson, A. J. Shields, P. Atkinson, K. Cooper, D. A. Ritchie, K. M. Groom, A. I. Tartakovskii, and M. S. Skolnick, Inversion of exciton level splitting in quantum dots. *Phys. Rev. B* **72**, 113305 (2005).
- [63] A. Mohan, M. Felici, P. Gallo, B. Dwir, A. Rudra, J. Faist, and E. Kapon, Polarization-entangled photons produced with high-symmetry site-controlled quantum dots. *Nature*

- Photonics* **4**, 302 (2010).
- [64] J. S. Bell, On the Einstein-Podolsky-Rosen paradox. *Physics* **1**, 195 (1964).
- [65] J. F. Clauser, M. A. Horne, A. Shimoni, and R. A. Holt, Proposed experiment to test local hidden-variable theories *Phys. Rev. Lett.* **23**, 880 (1969).
- [66] S. J. Freedman and J. F. Clauser, Experimental test of local hidden-variable theories. *Phys. Rev. Lett.* **28**, 938 (1972).
- [67] J. F. Clauser and M. A. Horne, Experimental consequences of objective local theories. *Phys. Rev. D* **10**, 526 (1974).
- [68] F. V. James, P. G. Kwiat, W. J. Munro, and A. G. White, Measurement of qubits . *Phys. Rev. A* **64**, 052312 (2001).
- [69] A. Peres, Separability Criterion for Density Matrices. *Phys. Rev. Lett.* **77**, 1413 (1996).
- [70] Y. Kodriano, E. Poem, N. H. Lindner, C. Tradonsky, B. D. Gerardot, P. M. Petroff, J. E. Avron, and D. Gershoni, Radiative cascade from quantum dot metastable spin-blockaded biexciton. *Phys. Rev. B* **82**, 155329 (2010).
- [71] E. Poem, Y. Kodriano, C. Tradonsky, B. D. Gerardot, P. M. Petroff, and D. Gershoni, Radiative cascades from charged semiconductor quantum dots. *Phys. Rev. B* **81**, 085306 (2010).
- [72] T. Warming, E. Siebert, A. Schliwa, E. Stock, R. Zimmermann, and D. Bimberg, Hole-hole and electron-hole exchange interactions in single InAs/GaAs quantum dots. *Phys. Rev. B* **79**, 125316 (2009).
- [73] E. Poem, S. Khatsevich, Y. Benny, I. Marderfeld, A. Badolato, P. M. Petroff, and D. Gershoni, Polarization memory in single quantum dots. *Solid State Commun.* **149** 1493 (2009).

- [74] A. Hartmann, Y. Ducommun, E. Kapon, U. Hohenester, and E. Molinari, Few-particle effects in semiconductor quantum dots: Observation of multicharged excitons. *Phys. Rev. Lett.* **84**, 5648 (2000).
- [75] M. H. Baier, A. Malko, E. Pelucchi, D. Y. Oberli, and E. Kapon, Quantum-dot exciton dynamics probed by photon-correlation spectroscopy. *Phys. Rev. B* **73**, 205321 (2006).